Current-induced re-entrant superconductivity and extreme nonreciprocal superconducting diode effect in valley-polarized systems

Yu-Chen Zhuang[1] **and Qing-Feng Sun**[1, 2⋆]

1 International Center for Quantum Materials, School of Physics, Peking University, 100871 Beijing, China
2 Hefei National Laboratory, Hefei, 230088 Anhui, China

⋆ sunqf@pku.edu.cn

Abstract

The superconducting diode effect (SDE) refers to the nonreciprocity of superconducting critical currents. Generally, the SDE has a positive and a negative critical currents $j_{c\pm}$ corresponding to two opposite directions with unequal amplitudes. It is demonstrated that an extreme nonreciprocity where two critical currents can become both positive (or negative) has been observed in twisted graphene systems. In this work, we theoretically propose a possible mechanism to realize an extreme nonreciprocal SDE. Based on a simple microscopic model, we demonstrate that depairing currents required to dissolve Cooper pairs can be remodulated under the interplay between valley polarizations and applied currents. Near the disappearance of the superconductivity, the remodulation is shown to induce extreme nonreciprocity and also the current-induced re-entrant superconductivity where the system has two different critical current intervals. Our study may provide new horizons for understanding the coexistence of superconductivity and spontaneous valley polarizations, and pave a way for designing SDE with 100% efficiency.

Received Date
Accepted Date
Published Date

Contents

---

1 Introduction

Superconducting diode effect (SDE) is a recently observed superconducting phenomenon with a nonreciprocity of the non-dissipative supercurrents [1,2], and has been attracting substantial attention. Such nonreciprocity means amplitudes of critical currents required to destroy the superconductivity are unequal in opposite directions. As a novel transport phenomenon, SDE can not only uncover underlying features in exotic superconducting systems [3, 4], but also serve as a non-dissipative circuit which has promising applications in low-power superconducting electronics [5], superconducting spintronics [6, 7], quantum information and communication technology [8, 9]. Since the observation of SDE in artificial superlattice $[\mathrm{Nb/V/Ta}]_\mathrm{n}$ [10], similar nonreciprocity of supercurrents has been observed in series of experiments, including bulk materials of diverse dimensions [11–16], Josephson junction devices [17–24], engineered superconducting structures [25, 26]. In theory, the rise of SDE usually relies on simultaneous breaking of time-reversal symmetry (TRS) and inversion symmetry [27–29], which is closely related to magnetochiral anisotropy [30–34], and finite-momentum Cooper pairings [35–38].

The performance of the SDE can be measured by the superconducting diode efficiency $\eta = \frac{j_{c+}-|j_{c-}|}{j_{c+}+|j_{c-}|}$, with the critical currents $j_{c\pm}$ for positive and negative directions [39, 40]. The value of η generally depends on the relevant system parameters like working temperature, applied magnetic field and chemical potentials [34, 41–43]. In most experiments, η can be optimized to several tens of percent. One notable exception appears in the experiment for zero-field SDE in small-twist-angle trilayer graphene where critical currents $j_{c\pm}$ are found to even cross zero and become both positive or negative at some regimes [15]. This so-called extreme nonreciprocity indicates a realization of SDE with 100% efficiency. It is a very counterintuitive feature since the electric current does not destroy superconductivity as traditionally believed, but rather promotes a normal state into a superconducting state. Some recent theoretical studies implies that the coupling between the symmetry-breaking order parameter and supercurrents could significantly enhance SDE efficiency η [44], and dissipations induced by the out-of plane electric field may falicite 100% SDE efficiency [45]. However, the emergence of extreme nonreciprocal SDE still remains an issue that requires further illuminations.

Due to its unique massless Dirac dispersion, the graphene system has been an excellent platform for exploring various novel physical phenomena [46–48]. Except for the charge and spin, the electrons in graphene have an additional degree of freedom, valley [49, 50]. In twisted graphene systems, a non-negligible phenomenon is that a dc current can modulate and even switch the valley polarization [51–56]. From the view of the bulk transport, the applied current can redistribute electron occupations in different valley bands near the Fermi level, and then induce energy band shifts due to the Coulomb interaction [53]. Considering the spontaneous valley polarization plays an important role in the SDE in twisted trilayer graphene, it is worth investigating the connection between the extreme nonreciprocal SDE and the current-induced valley polarization modulation.

In this work, based on the current-induced valley polarization modulation, we theoretically propose a possible mechanism to achieve the extreme nonreciprocity. By a simple valley-polarized system with intervalley pairings, we first study the nonreciprocity of intrinsic depairing current $\tilde{j}_c$ [41]. Then, we point out $\tilde{j}_c$ should be further remodulated to the actual critical current j_c because of the interplay between the current and valley occupations. In a large valley splitting regime close to the disappearance of superconductivity, this remodulation could lead to extreme nonreciprocity. The effects of variations of fillings and external magnetic fields on j_c are also investigated. Moreover, we raise a new phenomenon, the current-induced reentrant superconductivity, where the system has two different superconducting regions with distinct critical current intervals. Our study provides a possible routine to achieve SDE with 100% efficiency and also sheds light on the extreme nonreciprocity observed in the twisted graphene experiment.

The remainder of this article is organized as follows. In Sec. 2, we demonstrate our theoretical formalism to achieve the extreme nonreciprocity. In Sec. 2.1, we first construct a microscopic model to describe the spontaneous valley polarization. In Sec. 2.2, based on a simple valley-polarized model, we further show a physical mechanism to illustrate the current-induced valley polarization modulation. In Sec. 2.3, we study superconducting depairing currents and demonstrate a physical process to show how intrinsic depairing currents are remodulated as actual critical currents measured in the experiment. In Sec. 3, with a specific model, we use numerical calculations to verify our proposed physical mechanism. The critical currents before and after the remodulation, the variation of actual critical currents with electron occupations and external magnetic fields are investigated in detail, respectively. In Sec. 4, we give some discussions and a brief conclusion. The detailed formulations of the current-induced valley polarization modulation are shown in Appendix. A. In Appendix. B, we give some theoretical discussions to evaluate the self-consistent manner due to the effect of applied currents. In Appendix. C and D, we give some discussions about the trigonal warping effect and the coupling between supercurrents and valley polarizations. An estimation of the modulation coefficient $\alpha_{\pm}$ of currents and the effect of band asymmetry are shown in Appendix. E. The demonstration for the convergence of our results for the system size is put in Appendix. F.

2 Formalism

2.1 The mean-field model and the interaction-induced valley polarization

To depict the spontaneous valley polarizations, We simply consider a two-band Hamiltonian to implement a valley-polarized system with an intervalley interaction [53]:

$$H^{v} = \sum_{k,\tau} (\epsilon_{k,\tau} - \mu) c^{\dagger}_{k,\tau} c_{k,\tau} + \frac{U_v}{\mathcal{V}} \sum_{k,k'} c^{\dagger}_{k,+} c_{k,+} c^{\dagger}_{k',-} c_{k',-}, \tag{1}$$

where $\tau = \pm$ label the valley index K, K', $U_v > 0$ denotes the repulsive intervalley interaction. $\mathcal{V}$ and μ are the systemic size and chemical potential, respectively. $\epsilon_{k,\tau}$ denotes the single-particle band, which satisfies TRS: $\epsilon_{k,+} = \epsilon_{-k,-}$. Taking the mean-field approximation, the

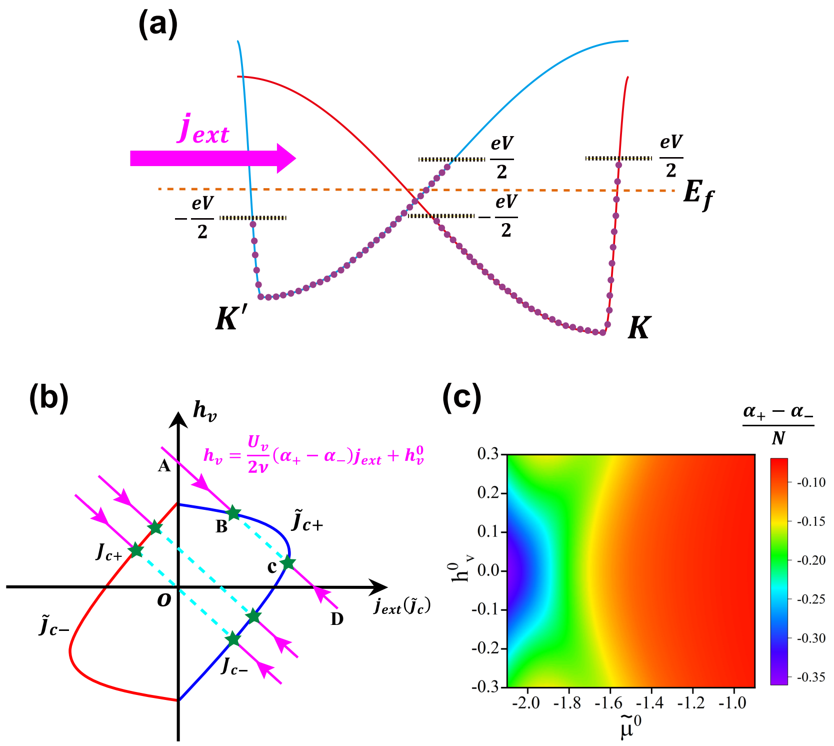

Figure 1: (a) Schematic illustration of the current-induced valley polarization modulation. The red and blue solid line denote two effective valley bands with the index $\tau = \pm$ (i.e., K, K'). The purple dots denote the occupied electrons on each band. Once an electric current j_{ext} (magenta arrow line) is applied, the local Fermi level for electrons with positive (negative) group velocities will climb (descend) by $eV/2$ relative to Fermi level E_f in equilibrium (black dashed lines). (b) The red and dark blue solid lines respectively denote intrinsic depairing currents $\tilde{j}_{c\pm}$ versus the valley splitting field h_v. The magenta solid lines and cyan dashed lines denote several h_v–j_{ext} relations of Eq. (5) with different h_v^0. At magenta solid lines, the system stays in the normal phase. While for cyan dashed lines, the system has entered the superconducting phase. The magenta arrows denote the direction of the phase transition starting from the normal phase to the superconducting phase, which is the focus of our theory. The intersection points (dark green stars) denote predicted actual critical currents $j_{c\pm}$. (c) The colormap for $(\alpha_+ - \alpha_-)/N$ versus h_v^0 and $\tilde{\mu}^0$.

Hamiltonian becomes $H_{MF}^v = \sum_{k,\tau} E_{k,\tau} c_{k,\tau}^\dagger c_{k,\tau} +$ const where $E_{k,\tau} = \epsilon_{k,\tau} - \mu + \frac{U_v}{\mathcal{V}} n_{-\tau}$. Here n_τ denotes the average electron occupation for τ valley: $n_\tau = \sum_k \langle c_{k,\tau}^\dagger c_{k,\tau} \rangle = \sum_k f(E_{k,\tau})$ with the Fermi distribution $f(E_{k,\tau}) = 1/(1+e^{\frac{E_{k,\tau}}{T}})$ (T is the thermal energy). The const $= -\frac{U_v}{\mathcal{V}} n_+ n_-$ is a constant arising from the mean-field approximation. Note that this mean-field model is similar to the rigid band flavor Stoner model with a $SU(4)$ symmetric Coulomb interaction energy $V_{int} \propto \sum_{\alpha \neq \beta} n_\alpha n_\beta$ (α,β denote four flavors $K\uparrow, K\downarrow, K'\uparrow, K'\downarrow$), which is often used to study flavor polarizations in graphene [57,58]. Since the valley polarization plays the most important role in the experiment [15], we first focus on valley flavors and neglect spin flavors.

It is easy to find that the growth of the electron occupation n_τ could lift the energy of $-\tau$ valley, and thus influence the free energy F_v of the system:

$$F_v(n,m) = -T \sum_{k,\tau} \ln(1+e^{-\frac{E_{k,\tau}}{T}}) - \frac{U_v}{4\mathcal{V}}(n^2 - m^2) + \mu n, \tag{2}$$

where $n = n_+ + n_-$ is the total electron occupation, $m = n_+ - n_-$ denotes the valley polarization. Generally, the system is fixed with a definite total electron occupation n and reaches a state where m is just the minimum point of the free energy $F_v(n,m)$. Therefore, the valley polarization can be solved by:

$$\frac{\partial F_v}{\partial m} = \frac{U_v}{2\mathcal{V}}\left(m - \sum_{k,\tau}\frac{\tau}{1+e^{\frac{E_{k,\tau}}{T}}}\right) = 0. \tag{3}$$

Once $U_v g(E_f)/\mathcal{V} > 1$ where $g(E_f)$ is the density of states at the Fermi level E_f, the strong repulsive Coulomb interaction overwhelms the kinetic energy and make the system favor a nonequal electron distribution between two valleys. This is analogous to the well-known Stoner criterion and at this time the solution m in Eq. (3) is nonzero [59]. The spontaneous valley polarization further introduces a valley splitting field $h_v = \frac{U_v m}{2\mathcal{V}}$ and a modified chemical potential $\tilde{\mu} = \mu - \frac{U_v n}{2\mathcal{V}}$ in mean-field bands $E_{k,\tau} = \epsilon_{k,\tau} - \tilde{\mu} - h_v \tau$.

2.2 The current-induced valley polarization modulations

In twisted graphene systems, it is found that a dc current could modulate and even switch the valley polarization [51–56]. We here illustrate it from a nonequilibrium ballistic quantum transport. In Fig. 1(a), the red solid line and blue solid line schematically correspond to two bands with valley K and valley K', respectively. Due to intervalley interaction, there is a spontaneous symmetry breaking as a consequence of two valley band splittings (e.g., the red band is below the blue band). Then, under an external bias V, an applied current j_{ext} (green arrow) will flow through the system and be carried by the energy bands. It leads to the Fermi level of electrons with positive (negative) velocities will rise (fall), for simplicity, $\frac{eV}{2}$ relative to the Fermi level E_f in equilibrium [60]. Moreover, if the valley bands are intravalley inversion symmetry-broken bands (i.e., $\epsilon_{k,\tau} \neq \epsilon_{-k,\tau}$), the variation of electron occupation for opposite velocities cannot be offset due to unequal density of states at the Fermi level, as indicated by purple dots (electron occupations) on colored solid lines in Fig. 1(a). Therefore, n_τ will be changed in each valley and is approximately proportional to j_{ext} at a small bias V (see detailed derivations in Appendix. A):

$$n_\tau = n_\tau^0 + \alpha_\tau j_{ext}. \tag{4}$$

The modulation coefficient α_τ is a function of the modified chemical potential $\tilde{\mu}$ and also the valley splitting field h_v. It relies on the difference between the positive and negative Fermi velocities and will be zero once $\epsilon_{k,\tau} = \epsilon_{-k,\tau}$ (see Appendix. A), which is again consistent with our picture shown in Fig. 1(a).

The variation of n_τ in Eq. (4) will further alter valley polarization $m = n_+ - n_-$ and the valley splitting field:

$$h_v = \frac{U_v}{2\mathcal{V}} m = \frac{U_v}{2\mathcal{V}}(\alpha_+ - \alpha_-) j_{ext} + h_v^0. \tag{5}$$

Here h_v^0 are the initial valley splitting field at $j_{ext} = 0$. It should be noted that the linear relation in Eq. (5) is only an approximation. In principle, the applied current j_{ext} which redistributes electron occupations in each valley can also refresh the value of h_v^0 simultaneously. The rigorous self-consistent calculation of h_v^0 including the nonequilibrium electric current is a subtle question. For simplicity, we focus on a small current range where the impact of j_{ext} on h_v^0 should be minor (see further discussions in Appendix. B). And thus in the calculations, we just ignore the influence of j_{ext} on h_v^0 in the right side of Eq. (5). We fix the modified chemical potential $\tilde{\mu} = \tilde{\mu}^0$ (considering the electron occupation is fixed) and ignore the dependence of $\alpha_\pm$ on h_v (consider the variation of h_v is not large at a small current). Then, the coefficient $\alpha_\pm$ on the right of Eq. (5) is just set as $\alpha_\pm(h_v^0, \tilde{\mu}^0)$, for simplicity.

The breaking of intravalley inversion symmetry on the energy bands could naturally exist in twisted graphene systems [53], as well as some materials with trigonal warping effect on the Fermi surface [61] (see more discussions in Appendix. C). Additionally, TRS guarantees opposite signs of $\alpha_{\pm}$. See Fig. 1(a), j_{ext} will make n_- larger and n_+ smaller, thereby reducing the valley polarization m and valley splitting field h_v.

2.3 The remodulation of critical currents and extreme nonreciprocity

Based on the valley-polarized system shown in Sec. 2.1, we further consider an s-wave finite-momentum intervalley pairing $H_s = -\frac{U_s}{\mathcal{V}}\sum_{k,q} c^{\dagger}_{k+q,+}c^{\dagger}_{-k+q,-}c_{-k+q,-}c_{k+q,+}$ in the system. Here $2q$ denotes the center-of-mass momentum of Cooper pairs. Although there is a competition between valley ferromagnetism and superconductivity, the traits of the coexistence between them have been found in twisted graphene systems [15,62]. To simplify the problem, we here consider the spontaneous valley polarization and superconducting pairing as two separate steps. At first, we regard the system as a normal state with valley-polarized bands determined from the mean-field solution in Eq. (1). Next, following ref. [41], we further add the s-wave intervalley pairing on it and now focus on its Bardeen-Cooper-Schrieffer (BCS) mean-field Hamiltonian for each fixed q:

$$H(q) = \sum_{k,\tau} E_{k,\tau} c^{\dagger}_{k,\tau} c_{k,\tau} - \sum_{k,q} \Delta(q) c^{\dagger}_{k+q,+} c^{\dagger}_{-k+q,-} + \text{H.c.} \tag{6}$$

where the first term is from the mean-field Hamiltonian of Eq. (1) and the second term denotes s-wave intervalley superconducting order parameter $\Delta(q)$, which should also be determined self-consistently. Note that $\Delta(q)$ in Eq. (6) corresponds to a periodic modulated order parameter $\Delta(x) = \Delta e^{i2qx}$ in space. A nonzero Cooper pair momentum in equilibrium state indicates a generation of a helical phase (Fulde-Fellel state) [42, 63–65]. Note that there is also a constant in Eq. (6) arising from the mean-field approximation for BCS mean-field Hamiltonian: const $= \sum_k E_{-k+q,-} + \frac{\mathcal{V}}{U_s}\Delta^2(q)$. It is neglected in Eq. (6) since it does not affect the following self-consistent calculation. Using Bogoliubov-de-Gennes (BdG) transformation, Eq. (6) can be further diagonalized as: $H(q) = \sum_k \tilde{E}_+(k,q)\alpha^{\dagger}_{k+q}\alpha_{k+q} + \tilde{E}_-(k,q)\beta_{-k+q}\beta^{\dagger}_{-k+q}$ with the eigenvalues $\tilde{E}_{\pm}(k,q) = E_1(k,q) \pm \sqrt{E_2^2(k,q)+\Delta^2(q)}$ and $E_{1,2}(k,q) = \frac{E_{k+q,+} \mp E_{-k+q,-}}{2}$. For every fixed q, $\Delta(q)$ should be self-consistently determined by a gap equation [41]:

$$\begin{aligned}
\Delta(q) &= \frac{U_s}{\mathcal{V}} \sum_k \langle c_{-k+q,-} c_{k+q,+} \rangle \\
&= -\frac{U_s}{\mathcal{V}} \sum_k \frac{\Delta(q)}{2\sqrt{E_2^2(k,q)+\Delta^2(q)}} (\langle \alpha^{\dagger}_{k+q}\alpha_{k+q}\rangle - \langle \beta_{-k+q}\beta^{\dagger}_{-k+q}\rangle) \\
&= -\frac{U_s}{\mathcal{V}} \sum_k \frac{\Delta(q)}{2\sqrt{E_2^2(k,q)+\Delta^2(q)}} [f(\tilde{E}_+(k,q)) - f(\tilde{E}_-(k,q))].
\end{aligned} \tag{7}$$

Based on $\Delta(q)$ in Eq. (7), we can calculate the free energy $\Omega(q)$ per volume:

$$\Omega(q) = \frac{\Delta^2(q)}{U_s} + \frac{1}{\mathcal{V}}\sum_k E_{-k+q,-} - \frac{T}{\mathcal{V}} \sum_{k,\eta=\pm} \ln(1 + e^{\frac{-\tilde{E}_\eta(k,q)}{T}}). \tag{8}$$

Following the previous derivations [41], the superconducting current flowing through the system j_s is evaluated as:

$$
\begin{aligned}
j_s(\Delta(q),q) &= \frac{e}{\hbar}\partial_q \Omega(\Delta(q),q) \\
&= \frac{e}{\hbar}\partial_q[\Omega(\Delta(q),q) - \Omega(\Delta(q)=0,q=0)] \\
&= \frac{e}{\hbar}\partial_q F_s(q).
\end{aligned} \tag{9}
$$

$F_s(q) = \Omega(\Delta(q),q) - \Omega(\Delta(q)=0,q)$ is the condensation energy per volume to quantize the difference of free energy density between the superconducting state and the normal state. In addition, the last equation uses the fact that $\Omega(\Delta(q)=0,q) = \Omega(\Delta(q)=0,q=0)$. Note that once $F_s(q) > 0$, we set it as zero regarding the superconducting phase is no longer stable. Eq. (9) actually follows the standard expression $j_s = -\partial_A \Omega$ with the gauge vector A [41,42]. In addition, the intrinsic depairing currents $\tilde{j}_{c\pm}$ just corresponds the global maximum $\tilde{j}_{c+} = \max_q[j_s(q)]$ and the global minimum $\tilde{j}_{c-} = \min_q[j_s(q)]$, respectively.

For the usual case, the depairing currents which are demanded to dissolve Cooper pairings are just equal to superconducting critical currents. No superconducting state can sustain once the applied normal current $j_{ext} > \tilde{j}_{c+}$ or $j_{ext} < \tilde{j}_{c-}$ for a definite valley polarization h_v. However, the situation becomes more complex after including the effect of the current-induced valley polarization modulation. See magenta solid lines and cyan dashed lines Fig. 1(b), as the applied current j_{ext} varies, the h_v will also change following the relation of Eq. (5). Note that h_v in turn affects the superconducting order parameter $\Delta(q)$ as well as corresponding depairing currents $\tilde{j}_{c\pm}(h_v)$ (red and dark blue solid lines). Therefore, the relations between j_{ext} and $\tilde{j}_{c\pm}$ should now be reevaluated. In Fig. 1(b), we use dark green stars to denote intersection points between the $h_v - j_{ext}$ line and the $\tilde{j}_{c\pm} - h_v$ lines. At the regions between these intersection points (cyan dashed lines), $|j_{ext}|$ is found to be always smaller than $|\tilde{j}_{c\pm}|$, indicating that the system should stay in the superconducting phase. While in the other regions (magenta solid lines), $j_{ext} > \tilde{j}_{c+}$ or $j_{ext} < \tilde{j}_{c-}$, meaning that the normal phase should be favored. Therefore, the intersection points can define actual critical currents $j_{c\pm}$ in metal-superconductor transitions. Moreover, we can find the characteristics of $j_{c\pm}$ strongly depends on the initial valley splitting field h_v^0 (intersections with the vertical axis). One notable example that the system stays in the normal phase at A point (magenta region) with $j_{ext} = 0$, but is driven into a superconductor (cyan region) after acrossing B point with $j_{ext} > 0$. This will lead to two positive critical currents ($j_{c\pm} > 0$), which is quite similar to extreme nonreciprocity observed in previous experiment [15].

One point may be noticed that the physical picture shown in Fig. 1(a) will not hold when the system has been driven into the superconducting phase (cyan regions) where the electron distribution is equilibrium. Actually, our work focuses on the process of driving the system into superconductivity with a normal current. The intersection points in Fig. 1(b) are still reasonable to define critical currents for the phase transition process starting from normal phases to the superconducting phases [denoted by the arrows in Fig. 1(b)]. Once crossing the intersection points (e.g., B point) from the magenta regions to cyan regions, the system cannot remain in the normal phase; otherwise, the normal current j_{ext} has to continue to weaken h_v along cyan dashed lines. At this time, the corresponding depairing currents $\tilde{j}_{c+}(h_v)$ allowed by the superconducting phase will inevitably exceed the applied normal current J_{ext}, indicating that the normal phase is no longer favored. This judgement does not yet involve the specific behaviors of currents and valley polarizations within the superconducting phase.

On the other hand, although the system has reached equilibrium when entering the superconducting phase, we emphasis equilibrium supercurrents can still couple to valley polarizations [44]. Similar to the Fig. 1(a), the finite momentum $2q$ of Cooper pairs carrying the

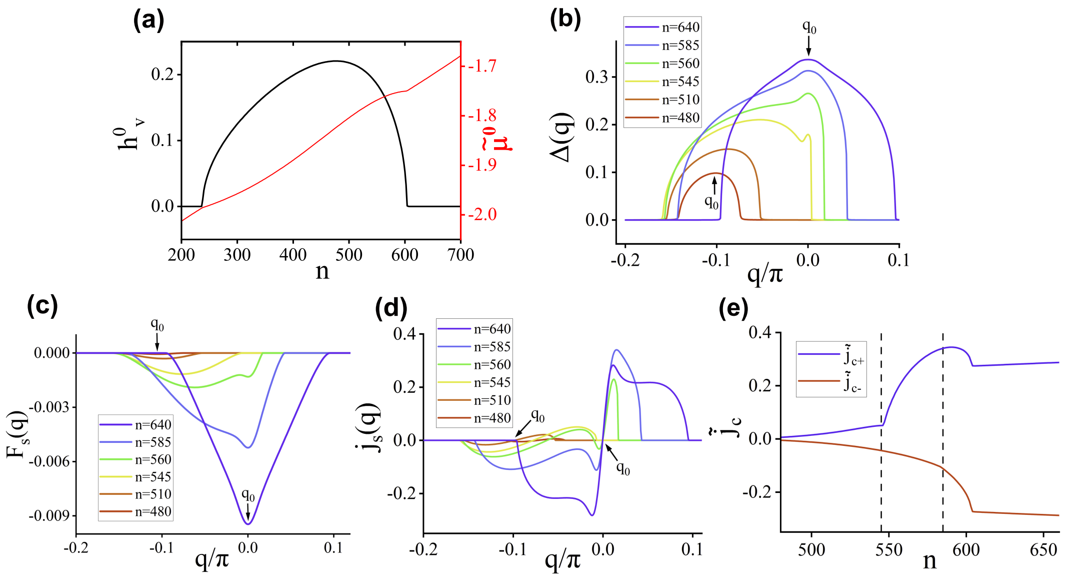

Figure 2: (a) The initial valley splitting field h_v^0 (dark line) and initial modified chemical potential $\tilde{\mu}^0$ (red line) versus the electron occupation n. (b, c, d) The distribution of superconducting order parameter $\Delta(q)$, the condensation energy $F_s(q)$ and supercurrent $j_s(q)$ for several n. (e) The variation of intrinsic deparing currents $\tilde{j}_{c\pm}$ versus the filling n.

supercurrent will also lift or lower the energy bands according to band dispersions. For valley bands with the broken intravalley inversion symmetry, this band shifts induced by Cooper-pair momentum cannot be simply offset, still leading to the change of valley polarizations (see some discussions in Appendix. D). Within the superconducting phases, the interplay between supercurrents-induced valley polarization modulations and superconductivity will also modulate critical currents.

In Eq. (5), a larger coefficient $\alpha_+ - \alpha_-$ implies j_{ext} can weaken h_v more quickly and drive the system into superconducting phase more easily. Below we choose a simple one-dimensional (1D) two-band toy model with $\epsilon_{k,+} = -2t\cos[\frac{8}{15}(k - \frac{7\pi}{8})]$ for $-\pi \leqslant k \leqslant \frac{7\pi}{8}$, $\epsilon_{k,+} = -2t\cos(8k - \pi)$ for $\frac{7\pi}{8} < k < \pi$, and $\epsilon_{k,+} = \epsilon_{-k,-}$. Similar model is used to illustrate the interplay between spontaneous valley polarization and applied currents, and could capture the asymmetric features of low-energy bands in twisted graphene [53]. In numerical calculations, $\mathcal{V} = Na$ with a periodic boundary condition and $N = 2000$. $t = 1$, $\frac{e}{\hbar}t = 1$, and $a = 1$ are set as energy, current and length units, respectively. We also set $U_v = 2.8$, $U_s = 1.86$ and thermal energy $T = 0.1$. In Fig. 1(c), the coefficient $(\alpha_+ - \alpha_-)/N$ versus the initial h_v^0 and $\tilde{\mu}^0$ is shown. $(\alpha_+ - \alpha_-)/N$ dives as $\tilde{\mu}^0$ becomes lower, considering Fermi velocities approach zero and α_τ becomes divergent near the bottom of bands. Furthermore, we also demonstrate a relatively significant $\alpha_+ - \alpha_-$ coefficient exist in a more realistic tight-binding model for twisted bilayer graphene. And the more asymmetrical the bands are, the larger $\alpha_+ - \alpha_-$ is (see both discussions in Appendix. E).

3 Numerical results

In this section, we will use a series of numerical calculations to validate our physical pictures illustrated in Fig. 1. We first study the initial valley splitting field h_v^0 and corresponding depairing currents $\tilde{j}_{c\pm}$ without the effect of current-induced valley polarization modulation, see

Sec. 3.1. Then, through the remodulation process shown in Fig. 1(b), we demonstrate actual critical currents j_c and explore the situation where the extreme nonreciprocity appears, see Sec. 3.2. We will also investigate the influence on j_c by the electron occupation n and the external magnetic field B, see Sec. 3.3.

3.1 The calculations without the effect of current-induced valley polarizations

For a given electron occupation n (or filling factor $\nu = n/N$), the initial $\tilde{\mu}^0$ and h_v^0 can be solved self-consistently from H_{MF}^{ν} and are shown in Fig. 2(a). Notice that $\pm h_v^0$ are degenerate solutions but we choose the positive one like the magnetic training in the experiment [15]. Here $\tilde{\mu}^0$ naturally declines as n decreases. Especially, a non-zero h_v^0 appears around $240 < n < 600$. Based on h_v^0, the $\Delta(q)$ is solved from the self-consistent gap equation in Eq. (7), and is shown in Fig. 2(b). As n declines from $n = 640$ to $n = 480$, h_v^0 becomes stronger and $\Delta(q)$ becomes weaker and more asymmetric with $\Delta(q) \neq \Delta(-q)$. This is because h_v^0 breaks TRS and destroys the Cooper pairs from intervalley pairings. Additionally, when $n < 545$, the strong h_v^0 causes that the center of $\Delta(q)$ wholely shifts from $q_0 = 0$ to $q_0 \approx -0.1\pi$, which apparently suggests Cooper pairs have large non-zero center of mass momenta [Fig. 2(b)].

Based on $\Delta(q)$, we also calculate corresponding condensation energy density $F_s(q)$, as shown in Fig. 2(c). As n changes from $n = 640$ to $n = 480$, the initial valley splitting field increases to break TRS and intervalley pairing, thus $F_s(q)$ becomes much more asymmetric and narrower. At around $n = 480$, $F_s(q)$ reaches almost zero and indicates superconductivity is highly unstable. Specially, a single-well structure of $F_s(q)$ with one global minimum assigning the ground state at $q_0 = 0$ ($n = 640$) gradually evolves into a double-well structure under a moderate valley splitting field (e.g. $n = 560$) with two local minimums. It goes back to the single-well structure with one minimum at $q_0 \approx -0.1\pi$ under a high valley splitting field (e.g. $n = 545$). Overall, the shift of the minimum point for $F_s(q)$ implies the superconductor transforms from a 'weak' helical phase to a 'strong' helical phase as the valley splitting field climbs [43].

We further estimate supercurrents $j_s(q)$ and depairing currents $\tilde{j}_{c\pm}$ versus n [Figs. 2(d, e)]. For about $n > 600$, j_s appears as an odd function with $\tilde{j}_{c+} = -\tilde{j}_{c-}$ since the initial valley splitting field h_v^0 is zero [Fig. 2(a)]. As n decreases, h_v^0 climbs and $j_s(q)$ becomes asymmetrical. $|\tilde{j}_{c-}|$ gradually decays while $\tilde{j}_{c+}$ lifts slightly because a small h_v^0 gives Cooper pairs finite momenta to flow towards one direction more easily [Fig. 2(e)]. By further decreasing n, two additional local extrema appear in $j_s(q)$ around a relatively high momentum $q_0 \approx -0.1\pi$ [Fig. 2(d)], and they successively become the new global minimum $\tilde{j}_{c-}$ ($n < 585$) and maximum $\tilde{j}_{c+}$ ($n < 545$) [denoted by black dashed lines in Fig. 2(e)]. Especially, the difference between $\tilde{j}_{c\pm}$ appears to be tiny after a transition from the 'weak' helical phase in low h_v^0 to the 'strong' helical phase in high h_v^0, see Figs. 2(c,d).

3.2 The actual critical currents through the remodulation process

Including the effect of current-induced valley polarization modulation, we state that depairing currents $\tilde{j}_c$ can be further remodulated as the actual critical currents j_c. As illustrated in Fig. 1(b), j_c can be determined by intersection points between the curve $\tilde{j}_c(h_v)$ and the curve $h_v(j_{ext})$. Note that j_{ext} and h_v have a definite relation in Eq. (5). Equivalently, we show diagrams with curves $\tilde{j}_{c,\pm}(j_{ext})$ (colored solid lines) and curves $\tilde{j}_c = j_{ext}$ (colored dashed lines) for four different n in Fig. 3.

In Fig. 3(a) with $n = 640$, h_v^0 is zero and depairing currents satisfy $\tilde{j}_{c+} = -\tilde{j}_{c-}$ at $j_{ext} = 0$. A non-zero applied current j_{ext} can evolve h_v to finite [inset in Fig. 3(a)], and simultaneously affect $\tilde{j}_{c\pm}$. While, intersection points still satisfy $j_{c+} = -j_{c-}$ indicating no SDE (dark green stars), due to the fact that $\tilde{j}_{c+}(h_v) = -\tilde{j}_{c-}(-h_v)$ and $h_v(j_{ext}) = -h_v(-j_{ext})$ at this case.

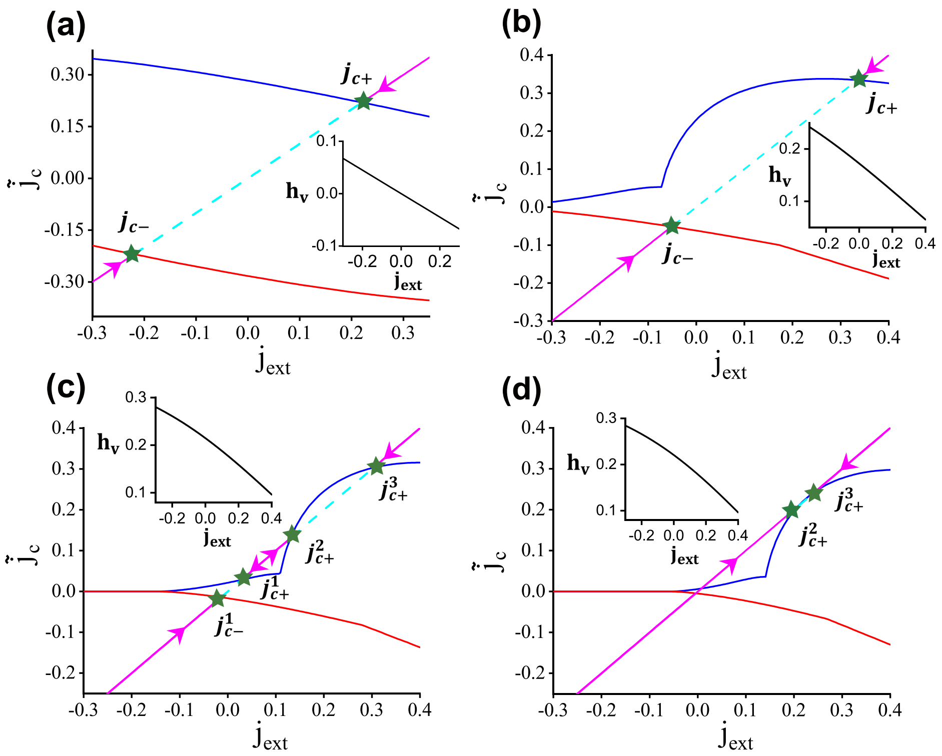

Figure 3: (a-d) The intrinsic depairing currents $\tilde{j}_c$ (main panels) and h_v versus j_{ext} (insets) for $n = 640$ (a), $n = 560$ (b), $n = 510$ (c) and $n = 480$ (d). The intersection points (dark green stars) between the $\tilde{j}_{c,\pm} - j_{ext}$ (red and dark blue solid lines) and $\tilde{j}_c = j_{ext}$ (magenta solid lines and cyan dashed lines) are $j_{c,\pm}$. Similar to Fig. 1(b), the magenta parts denote the regions of the normal phases and the cyan parts denote the regions where the systems eventually transition into superconducting phases. The magenta arrows denote the phase transition from normal states to superconducting states that our theory focuses.

When $n = 560$, a small h^0_v appears and $\tilde{j}_{c+} \neq |\tilde{j}_{c-}|$ at $j_{ext} = 0$ in Fig. 3(b). The forward current ($j_{ext} > 0$) reduces h_v while the backward current ($j_{ext} < 0$) enhances the h_v[inset in Fig. 3(b)]. SDE persists with two modified $j_{c\pm}$ (dark green stars). When $n = 510$ [Fig. 3(c)], h^0_v is relatively strong and the system enters a 'strong' helical superconducting phase as indicated by Figs. 2(c,d). The depairing currents $\tilde{j}_{c\pm}$ are relatively small at $j_{ext} = 0$.

Interestingly, since there is a sudden change in the slope of curve $\tilde{j}_{c+}(j_{ext})$ [as indicated in Fig. 2(e)], the number of intersection points could be four, which are symbolized by four actual critical currents (j^1_{c-} and j^{1-3}_{c+}). Regarding that there exist two different superconducting phases with two distinct critical current intervals [67], We call this phenomenon as current-induced re-entrant superconductivity. Once h^0_v becomes too large [see Fig. 3(d) with $n = 480$], $j^1_{c\pm}$ obviously shrink towards zero and hard to be measured in the experiment, while $j^{2,3}_{c+}$ persist. Now it exhibits the extreme nonreciprocity only with two positive actual critical currents.

Similar to the schematic diagram in Fig. 1(b), we use magenta solid lines to mark normal phase regions and use cyan dashed lines to denote superconducting regions in Fig. 3. Following the magenta arrows, when the system is initially prepared in normal phases (magenta regions) and driven by the normal current to cross intersection points, the normal phase cannot be maintained, otherwise h_v will continue to be weakened along the cyan dashed line. Our theory focuses on the current-induced phase transition from normal phases to superconducting phases and offers a possible mechanism for the observation of extreme nonreciprocal SDE in ref. [15].

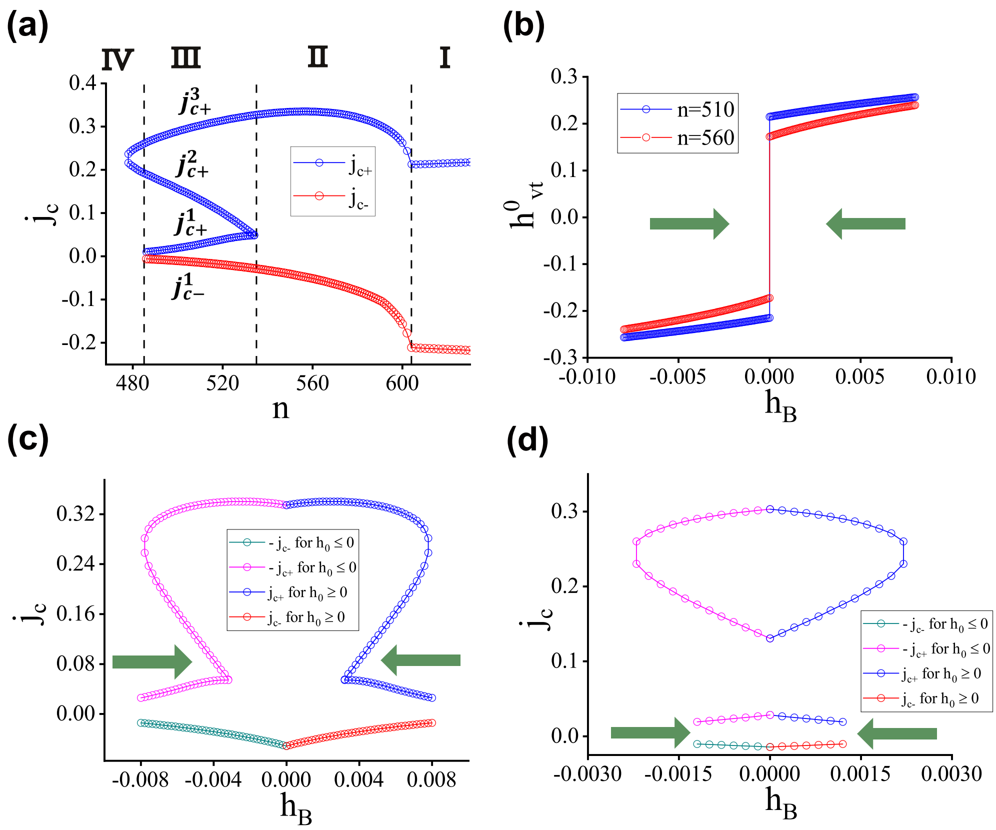

Figure 4: (a) The variation of $j_{c\pm}$ as a function of n. (b) The modulation of the total valley splitting field h^0_{vt} with h_B induced by the external magnetic field. (c,d) $j_{c\pm}$ versus h_B for $n = 560$ (c) and $n = 510$ (d) [66]. The dark green arrows denote the scanning directions of the magnetic field B or h_B.

Additionally, when the system stays in the superconducting phase, the supercurrents will still couple to supercurrents [44]. As the supercurrent-induced valley polarization modulation is not completely the same as the normal current case, there may be a hysteresis behaviour when the system in turn transitions from the superconducting phase and the normal phase.

3.3 The variation of actual critical currents with different parameters

To study the SDE comprehensively, in Fig. 4(a) we extract $j_{c\pm}$ based on the intersection points in Fig. 3 and show them in a wide range of electron occupations n. Here four regions are denoted. In region **I**, the system does not exhibit SDE due to zero h^0_ν. In region **II**, h^0_ν is moderate and the conventional SDE with $j_{c+} \neq |j_{c-}|$ is observed. $j_{c+} - |j_{c-}|$ becomes roughly larger as n decreases (h^0_ν climbs). In region **III**, h^0_ν is relatively large. The system exhibits re-entrant superconductivity with four actual critical currents (j^1_{c-} and j^{1-3}_{c+}). In region **IV**, h^0_ν is stronger and $j^1_{c\pm}$ become too small to be observed. Only $j^{2,3}_{c+}$ are left and thus the system exhibits an obvious extreme nonreciprocity. When h^0_ν grows to too large (n is small), both $j^{2,3}_{c+}$ will disappear and the superconducting phase cannot exist. The extreme nonreciprocity occurs near the disappearance of superconductivity in our theory is akin the feature in ref [15].

Besides varying fillings, we also investigate how an external magnetic field B can modulate $j_{c\pm}$. Enlightened by ref. [15], we now consider the valley τ is locked with the spin s_z, which can arise from the Ising spin-orbit coupling [68, 69]. Thus, B can couple to valley through a Zeeman effect and induce an additional valley splitting field $h_B \propto B$ into the Hamiltonian

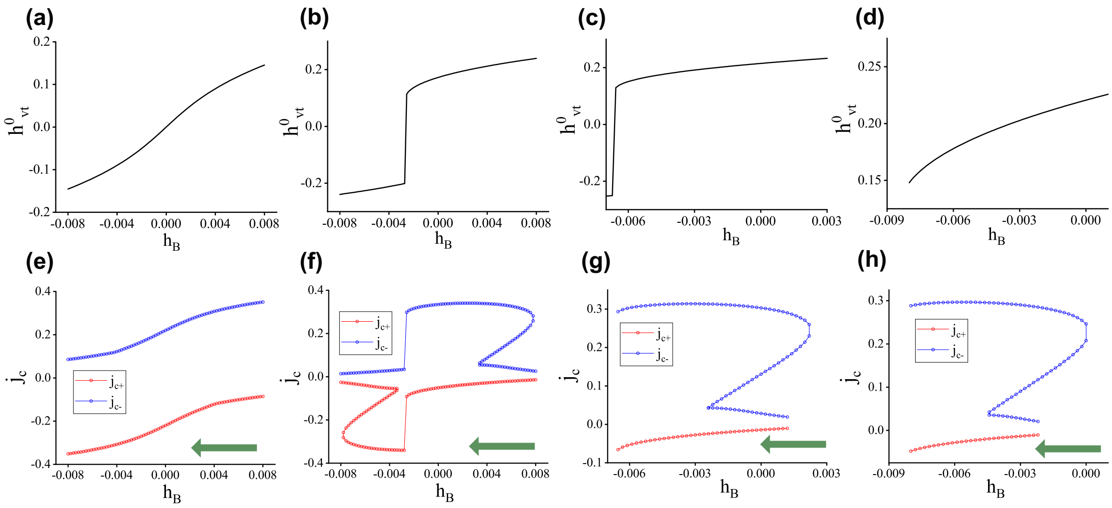

Figure 5: (a-d) The change of the total valley splitting field h_{vt}^0 as a function of the h_B for electron occupation $n = 640$ (a), $n = 560$ (b), $n = 510$ (c) and $n = 480$ (d). The system is initially prepared at the stable state at $m \geq 0$ without the external magnetic field B. And the magnetic field as well as the additional valley splitting field h_B is scanned from positive to negative which influences the self-consistent result h_{vt}^0 in every step. (e-h) the change of the actual critical currents j_c as a function of h_B, corresponding to the cases in (a-d), respectively. The dark green arrows denote the scanning direction.

$H_{MF}^{v} = \sum_{k,\tau}(E_{k,\tau} - h_B\tau)c_{k,\tau}^{\dagger}c_{k,\tau}$. Through similar self-consistent calculations in Eq. (3), the total valley splitting field $h_{vt}^0 = h_v^0 + h_B$ is refreshed along with the magnetic field.

In Fig. 4(b), we plot the calculated h_{vt}^0 versus h_B. Note that here the system is initially prepared at $h_v^0 > 0$ ($h_v^0 < 0$) before applying the magnetic field $B > 0$ ($B < 0$). It roughly corresponds to magnetic field B scanned from positive (negative) direction to zero (see dark green arrows). Actually, these two cases are antisymmetric due to TRS. We can find $|h_{vt}^0|$ decays as $|h_B|$ weakens, reflecting the modulation of valley polarizations by the external magnetic field. We also plot j_c versus h_B for two distinct n. For $n = 560$ in Fig. 4(c), as h_B sweeps from positive to zero, the decay of h_{vt}^0 drives the number of actual critical currents from 4 to 2. It means, the system evolves from a re-entrant superconducting phase to a conventional SDE. For $n = 510$ in Fig. 4(d), the system is initially an extreme nonreciprocal SDE with two positive j_c at $|h_B| \approx 0.002$. The decline of $|h_B|$ pulls down h_{vt}^0 and impels the system into re-entrant superconducting phase with four distinct j_c.

Additionally, the polarity of SDE may be also reversed when scanning B from the positive to negative direction, see Fig. 5. At these cases, the system is initially prepared at $m \geq 0$ for $n = 640$ [Figs. 5(a,e)], $n = 560$ [Figs. 5(b,f)], $n = 510$ [Figs. 5(c,g)] and $n = 480$ [Figs. 5(d,h)], respectively. Then, we apply and scan $h_B \propto B$ from positive to negative (dark green arrows). For $n = 640$, since no valley polarization appears without the external magnetic field ($h_B = 0$), both the sign of h_{vt}^0 and the polarity of SDE correlates well with h_B [Figs. 5(a,e)]. For the case of $n = 560$ and $n = 510$, a sudden sign change of h_{vt}^0 appears as h_B reaches about -0.0027 [Fig. 5(b)] and -0.007 [Fig. 5(c)]. This switching could also reverse the polarity of SDE in Fig. 5(f). Note that the switching of h_{vt}^0 in Fig. 5(c) is so large that $j_{c\pm}$ disappears in Fig. 5(g). Similar to Fig. 4, the number of j_c also varies with h_B which manifests the transformation of types of SDE [Figs. 5(f,g)]. Since the initial valley splitting field h_v^0 for $h_B = 0$ is too large for $n = 480$, a small variation of magnetic field is not enough to switch total valley splitting field h_{vt}^0 [Fig. 5(d)]. But the superconducting phase gradually transforms from an extreme nonreciprocity with two positive j_c to the re-entrant superconductivity with four j_c and then to the conventional SDE with $j_{c+} > 0, j_{c-} < 0$ [Fig. 5(h)].

In summary, our results in Fig. 4 and Fig. 5 both demonstrate that the extreme nonreciprocity can occur and be adjusted by the variation of the electron occupation n and the external magnetic field B. Additionally, our results are robust to changes in system size (see Appendix. F).

4 Discussions and conclusion

The toy model we calculated can qualitatively explain the phenomena observed in experiments. In fact, through a rough estimation, we also find that the calculated results are also similar in magnitude to experimental measurements. Considering a narrow bandwidth of the flat band with $4t = 10$ meV [70–73], the energy unit becomes $t = 2.5$ meV and the current unit becomes $\frac{e}{\hbar}t \approx 96.6$ nA. Thus, the set temperature T in the unit of Kelvin is around 2.9 K. In Fig. 2, the initial valley splitting field h_v^0 varies from 0 to about $0.2t$ (0.5 meV) and the maximal superconducting order parameter is $\Delta \approx 0.33t \approx 0.83$ meV. In Fig. 4(a), we can roughly estimate the amplitudes of critical currents $j_{c\pm}$ varying from 0 to 34 nA, which is in order of magnitude consistent with the previous experiment results [15]. It is also worth noting that the normal currents arranging from several nA to tens of nA is experimentally confirmed to be able to affect magnetizations in twisted bilayer graphene [51, 52], which are still similar in magnitudes for current-induced valley polarization modulations in our theoretical scheme. Totally speaking, the modulation of valley splitting field caused by the weak current is not strong in our results. See Fig. 3, h_v changes by about $0.1t$ (about 0.25 meV) as the current changes by about $0.4\frac{e}{\hbar}t$ (about 40 nA).

In conclusion, based on a simple valley-polarized model, we have revealed that intrinsic depairing currents can be remodulated due to the current-induced valley polarization modulation. Depending on specific features, we have demonstrated that such a remodulation can induce the extreme nonreciprocity and also the current-induced re-entrant superconductivity. These special SDE can be further adjusted by varing electron occupations and external magnetic fields. Our study reflects the peculiarity in the interplay between valley ferromagnetism and superconductivity, provide a possible mechanism to explain experimental observations of extreme nonreciprocal SDE and open a new way to implement SDE with 100% efficiency.

Acknowledgements

We are grateful to Yue Mao and Yi-Xin Dai for fruitful discussions.

Funding information This work was financially supported by the National Natural Science Foundation of China (Grant No. 12374034 and No. 11921005), the National Key R and D Program of China (Grant No. 2024YFA1409002), Quantum Science and Technology-National Science and Technology Major project (2021ZD0302403), the China Postdoctoral Science Foundation (No. 2025T180938) and the Postdoctoral Fellowship Program of CPSF under Grant Number GZB20240031. We also acknowledge the High-performance Computing Platform of Peking University for providing computational resources.

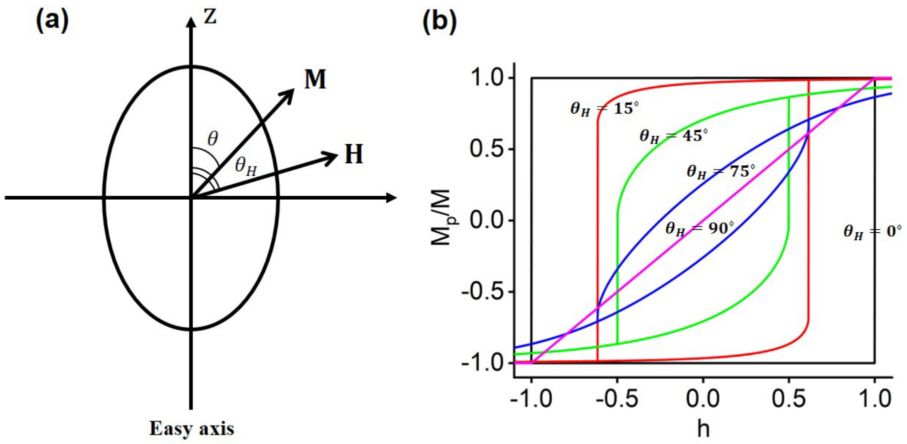

Figure 6: (a) The model for a single-domain spheroidal particle endowed with uniaxial magnetic anisotropy. The magnetization M is aligned with an angle θ between the easy axis z and the external magnetic field H is aligned with an angle θ_H between the easy axis z. (b) The numerical calculated magnetization curves between M_p/M and h for different angles θ_H.

395 ## A Formulations of the current-induced valley polarization modu-
396 lation

397 When the applied current j_{ext} flows through the valley-polarized system shown in Eq. (1),
398 occupations for electrons with opposite group velocities should be further imbalanced. In
399 detail, taking a 1D system shown in Fig. 1(a) as an example with $\mathcal{V} = Na$ where $a = 1$ is the
400 length unit, the Fermi level of electrons with positive (negative) velocities, coming from the
401 source (drain) will rise (fall) $\frac{eV}{2}$, respectively. Then, the electron occupation n_τ on each valley
402 τ changes into:

$$n_\tau = \sum_k f[\epsilon_{k,\tau} - \tilde{\mu} - h_v\tau - \frac{eV}{2}\text{sgn}(\epsilon'_{k,\tau})] \tag{A.1}$$

403 with $\text{sgn}(x > 0) = 1, \text{sgn}(x = 0) = 0, \text{sgn}(x < 0) = -1$. And e is the electron charge. For a
404 small bias $V \to 0$, Eq. (A.1) can be further approximated as:

$$n_\tau \approx n_\tau^0 - \frac{eV}{2}\sum_k \text{sgn}(\epsilon'_{k,\tau})f'(\epsilon_{k,\tau} - \tilde{\mu} - h_v\tau), \tag{A.2}$$

405 where $n_\tau^0 = \sum_k f(\epsilon_{k,\tau} - \tilde{\mu} - h_v\tau)$ is the original electron occupation before applying the current
406 j_{ext}. Furthermore, the current j_{ext} flowing through the system which is closely related to the
407 voltage V can be also calculated:

$$\begin{aligned} j_{ext} &= \frac{e}{\hbar N}\sum_{k,\tau}\epsilon'_{k,\tau} f[\epsilon_{k,\tau} - \tilde{\mu} - h_v\tau - \frac{eV}{2}\text{sgn}(\epsilon'_{k,\tau})] \\ &\approx \frac{e}{h}\int dk \sum_\tau \epsilon'_{k,\tau} f[\epsilon_{k,\tau} - \tilde{\mu} - h_v\tau - \frac{eV}{2}\text{sgn}(\epsilon'_{k,\tau})]. \end{aligned} \tag{A.3}$$

408 Here we regard the $N \to \infty$ and thus the summation of k changes into the integral for simplic-
409 ity. Similarly, when the bias is small with $V \to 0$, the current in Eq. (A.3) can be approximated
410 as:

$$j_{ext} \approx \frac{e^2V}{h}\sum_\tau [-f(\epsilon_{k,\tau}^{max} - \tilde{\mu} - h_v\tau) + f(\epsilon_{k,\tau}^{min} - \tilde{\mu} - h_v\tau)], \tag{A.4}$$

where $\epsilon_{k,\tau}^{max}$ and $\epsilon_{k,\tau}^{min}$ is the global maximum and minimum value of $\epsilon_{k,\tau}$. For a low temperature $T \to 0$ and $\tilde{\mu} \in (\epsilon_{k,\tau}^{min} - h_v\tau, \epsilon_{k,\tau}^{max} - h_v\tau)$, $j_{ext} = \frac{2e^2V}{h}$ well corresponds to Landauer-Büttiker formula in a ballistic regime [60]. Substituting Eq. (A.4) into Eq. (A.2), we can get the relation between n_τ and j_{ext} as

$$n_\tau = n_\tau^0 + \alpha_\tau j_{ext}, \tag{A.5}$$

and also the change of valley splitting field h_v:

$$h_v = \frac{U_v}{2\mathcal{V}}(n_+ - n_-) = \frac{U_v}{2\mathcal{V}}(\alpha_+ - \alpha_-)j_{ext} + h_v^0 \tag{A.6}$$

where h_v^0 is the initial valley splitting field when $j_{ext} = 0$. The Eq. (A.6) is just Eq. (3) in the main text. The coefficient α_τ to measure the ability for the current to modulate the valley polarization is a function of modified chemical potential $\tilde{\mu}$ and valley splitting field h_v:

$$\begin{aligned} &\alpha_\tau(\tilde{\mu}, h_v) \\ &= \frac{h\sum_k \mathrm{sgn}(\epsilon'_{k,\tau})f'(\epsilon_{k,\tau} - \tilde{\mu} - h_v\tau)}{2e\sum_\tau[f(\epsilon_{k,\tau}^{max} - \tilde{\mu} - h_v\tau) - f(\epsilon_{k,\tau}^{min} - \tilde{\mu} - h_v\tau)]}. \end{aligned} \tag{A.7}$$

During applying an electric current j_{ext}, the change of h_v and $\tilde{\mu}$ could alter the value of α_τ in time. For simplicity, we ignore this effect and directly set $\alpha_\tau(\tilde{\mu}, h_v)$ as $\alpha_\tau(\tilde{\mu}^0, h_v^0)$. The detailed distribution of $\alpha_\tau(\tilde{\mu}^0, h_v^0)$ for an 1D toy model in Sec. 2.3 is shown in Fig. 1(c). Note that its unit is h/et.

Especially when $T \to 0$, $\alpha_\tau \propto \sum_n \frac{1}{\epsilon'_\tau(k_F^n)}$ where k_F^n is the n-th Fermi wave vector at the Fermi level E_f. Thus, the value of α_τ is closely related to the inverse of Fermi velocities $v_F^n = \frac{1}{\hbar}\epsilon'_\tau(k_F^n)$. If the energy band has the intravalley inversion symmetry: $\epsilon_{k,\tau} = \epsilon_{-k,\tau}$. It leads to $\epsilon'_{k,\tau} = -\epsilon'_{-k,\tau}$ and α_τ as well as the change in Eq. (A.6) should be canceled to be zero. The necessity of intravalley inversion breaking is consistent with the finding in ref. [53]. In addition, the intravalley inversion symmetry breaking is also found as a crucial condition to realize the SDE in the valley polarized system [61]. This coincidence implies the possibility for the combination between the current-induced valley polarization modulation and SDE.

In numerical calculations, we do not directly use the α_τ to obtain the results of current-induced valley modulation in Eq. (A.6). To be more accurate, after given the applied current I_{ext}, we use Eq. (A.4) to obtain the corresponding bias energy eV. Then we bring eV into Eq. (A.1) to get the electron occupation n_τ on each valley and also use $h_v = \frac{U_v}{2\mathcal{V}}(n_+ - n_-)$ to obtain the corresponding h_v. Note that the modified chemical potential $\tilde{\mu}$ and the valley splitting field h_v are fixed as $\tilde{\mu}^0$ and h_v^0 in the right parts in Eq. (A.1)—Eq. (A.4). In Eq. (A.1), we do not assume that the bias eV is small, so that $h_v = \frac{U_v}{2\mathcal{V}}(n_+ - n_-)$ versus the bias eV deviates slightly from the linear relation (see the insets of Fig. 3).

B The self-consistent manner including the effect of applied currents

In the main text, we set the total valley polarization in Eq. (5) is the summation of the current-induced part and the spontaneous polarization part from the Coulomb interaction. The influence on h_v^0 by the applied current j_{ext} is just neglected. In this Appendix, we will discuss this self-consistent process theoretically and demonstrate the rationality of our linear approximation in Eq. (5) for a small j_{ext}.

Actually, Eq. (5) is easy to recall from the relationship between the magnetic induction $\mathbf{B}$ and magnetic field strength $\mathbf{H}$:

$$\mathbf{B}/\mu_0 = \mathbf{M} + \mathbf{H}. \tag{B.1}$$

where **M** is the magnetization and μ_0 is the permeability of free space. Neglecting the coefficients, j_{ext}, h_v^0 and h_v in Eq. (5) just corresponds to **H**, **M** and **B** in Eq. (B.1), respectively. In the magnetization process, the external magnetic field strength **H** could also affect the intrinsic magnetization **M**(**H**), causing the relationship between **B** and **H** more complicated, usually along with magnetic hysteresis loops. Based on a rough analogy, we can draw on the magnetic curve of $M = F(H)$ to further speculate the behaviors of $h_v^0 = F(I_{ext})$.

Strictly speaking, spin and valley cannot be simply equivalent, considering there are some differences between them. Thus, the analogy between valley and spin is just a crude mean to help understanding. However, given that valley and spin also have some similarities in our model, this analogy is still plausible to some extent. At first, our theory is simply built on a two-band Stoner Hamiltonian where valley only serves as a flavor degree of the energy bands. In principle, replacing the valley index with the spin index has no intrinsic influence on our theoretical analysis and the physical picture in Fig. 1. In some previous studies in graphene systems, the polarization of spin and valley flavors is often regarded as isospin magnetism as a whole [58, 74]. Secondly, the spin and valley are found to be locked together due to the presence of proximity-induced Ising SOC [15], which also indicates the effect of valley and spin has some equivalence in the experiment.

In the following part, we will explain the influence on h_v^0 by j_{ext} based on two fashioned theoretical perspectives: Stoner-Wohlfarth model and Rayleigh law.

To analyze the function of $h_v^0 = F(I_{ext})$ from Stoner-Wohlfarth model. The theory of Stoner-Wohlfarth model is based on the coherent rotation of the magnetization in a single-domain particle [75]. This is a simple theoretical model, but it could illustrate the rationality of our approximation to some extent. As shown in Fig. 6 (a), a spheroidal single-domain particle endowed with uniaxial anisotropy. The magnetization **M** is aligned with an angle θ between the easy axis. The internal energy density is expressed as a function of θ as [76]:

$$u_{an}(\theta) = K_u \sin^2(\theta). \tag{B.2}$$

Here K_u is the anisotropy parameter which is related to the magnetocrystalline anisotropy and shape effects. Then we consider the single domain subjected an applied magnetic field **H** making the angle θ_H with the easy axis, and the field interaction energy density is [76]:

$$u_H(\theta) = -\mu_0 MH \cos(\theta_{\mathrm{H}} - \theta). \tag{B.3}$$

Thus, the total Gibbs free energy density is:

$$g(\theta) = u_{an}(\theta) + u_H(\theta) = K_u \sin^2(\theta) - \mu_0 MH \cos(\theta_H - \theta). \tag{B.4}$$

Note that here we only pay attention on the coherent rotation of **M** with the strength of **M** unchanged. And the value of **H** oscillating between positive and negative values with θ_H varying between 0° and 90°. The equilibrium conditions are obtained as $g(\theta)$ reaches the minimum. For convenience, we reduce the $g(\theta)$ as $\tilde{g}(\theta) = g(\theta)/(2K_u)$. The equilibrium conditions are:

$$\frac{d\tilde{g}}{d\theta} = \frac{1}{2}\sin(2\theta) - h\sin(\theta_H - \theta) = 0 \tag{B.5a}$$
$$\frac{d^2\tilde{g}}{d^2\theta} = \cos(2\theta) + h\cos(\theta_H - \theta) > 0. \tag{B.5b}$$

where $h = \mu_0 MH/2K_u = H/H_K$. The solution of Eq. (B.5) can be studied analytically in some cases. For example, when $\theta_H = 0$, the magnetic field **H** is aligned with the easy axis, and the solution of Eq. (B.5a) is $\sin(\theta) = 0$ and $\cos(\theta) = -h$. For the first case, $\theta = 0, \pi$ and

Eq. (B.5b) gives $\frac{d^2\tilde{g}}{d^2\theta} = 1 \pm h > 0$. For the second case, $\theta = \arccos(-h)$ and Eq. (B.5b) gives $\frac{d^2\tilde{g}}{d^2\theta} = h^2 - 1 > 0$. In general, $h < -1, \theta = \pi$; $h > 1, \theta = 0$; $-1 \le h \le 1, \theta = 0$ or π (depending on the initial path). To further demonstrate, we plot the magnetization resolved in the field direction $M_p(\theta_H) = M\cos(\theta_H - \theta)$ under the cyclic variation of the field $h = H/H_K$ in Fig. 6(b) with $\theta_H = 0°, 15°, 45°, 75°, 90°$. The Fig. 6(b) is numerically calculated from Eq. (B.5). It can be found that a change in h causes hysteresis loops where M_p can be reversed at certain critical value h_c (i.e. the coercive field). The characteristics of hysteresis loops are strongly dependent on the aligned angle θ_H of **H**. For $\theta_H = 0$, we can find a square hysteresis loop with $M_p = \pm M$ [see the black solid line in Fig. 6(b)]. For the larger θ_H, the hysteresis loop shrinks and finally becomes a linear function at $\theta_H = 90°$ [see the magenta solid line in Fig. 6(b)]. For an isotropic system of randomly oriented identical particles, the overall mean behaviour stems from an averaged hysteresis loop for different angles.

Next, we refer to the $M_p = F(H)$ of the Stoner-Wohlfarth model shown in Fig. 6(b), and analyze the relationship $h_v^0 = F(I_{ext})$. There is a difference between the valley-polarization and the magnetization in ferromagnets. For the latter, a spin-rotation symmetry is maintained and the ferromagnetism is described by a vector order parameter. In contrast, the valley polarization in our system is Ising-like and not a vector [54]. The system is either polarized at K valley or K' valley, but never polarized at a valley-coherence state like $\frac{1}{\sqrt{2}}(|K\rangle + |K'\rangle)$. This means the direction of the valley polarization is only aligned along the easy axis (z axis). In addition, since the applied current I_{ext} will influence the valley polarization but cannot mix two valleys, the effect of I_{ext} should be analogous to the effect of **H** at $\theta_H = 0°$. Therefore, the curve of $h_v^0(I_{ext})$ should be similar to the curve of $M_p(H)$ at $\theta_H = 0°$ as shown by black solid lines in Fig. 6 (b) in a small single-domain valley-polarized system. Actually, even if in a multi-domain system, the averaged hysteresis loop could be somehow like the curve at $\theta_H = 0°$, because the easy axis of each domain is along the z direction. Therefore, we can conclude that h_v^0 remains nearly unchanged as long as I_{ext} is not too large. Considering the current to flip the valley polarization sometimes demands to reach several tens of nA [51], which is basically larger than the critical currents obtained by our numerical calculations, our linear approximation in Eq. (5) has some rationality.

To analyze the function of $h_v^0 = F(I_{ext})$ from the Rayleigh law. For a further comparison, we next refer to another theory called as Rayleigh law, which is used to describe the behavior of ferromagnetic materials at low fields [77, 78]. The Rayleigh law is a technical model describing the magnetic hysteresis phenomenon with simple mathematical functions. It quantizes the initial magnetization curve as a second order equation [79]:

$$B(H) = aH + bH^2. \tag{B.6}$$

Here a corresponds to reversible part of the magnetization process with $a = \lim_{H\to 0} \frac{\partial B}{\partial H} = \mu_0 \mu_i$ (μ_i is the initial permeability), and b corresponds to the irreversible part of the magnetization process. Based on this initial magnetization curve, Rayleigh law describes the magnetic hysteresis loop by two symmetrical, intersecting parabolic curves [79]:

$$B(H) = (a + bH_m)H \pm \frac{b}{2}(H_m^2 - H^2). \tag{B.7}$$

Note that this function describes the behavior of magnetic induction B with the magnetic field H. H_m is the amplitude of the scanning magnetic field during the magnetization process. The '+' sign denotes the upper branch of the loop, while the '-' sign denotes the lower branch of the loop. We can draw an analogy from Eqs. (B.6, B.7), and give the innitial valley polarization curve and the hysteresis for h_v as a function of the applied current j_{ext}, respectively:

$$h_v(j_{ext}) = a j_{ext} + b j_{ext}^2 \tag{B.8a}$$

$$h_v(j_{ext}) = (a + b j_{ext,m}) j_{ext} \pm \frac{b}{2}(j_{ext,m}^2 - j_{ext}^2). \tag{B.8b}$$

Similarly, $j_{ext,m}$ is the amplitude of scanning current, i.e. Eq. (B.8b) is valid when $|j_{ext}| \leq j_{ext,m}$. Once $j_{ext,m}$ is fixed, the form of $h_v(j_{ext})$ is determined by the parameter a and b.

In general, the value of a and b can be obtained by experimental fittings. Here, we try to estimate them theoretically. According to Eq. (B.6), the parameter a reflects the reversible part of the initial magnetization curve, which shows the relationship between H and M as the field strength is increased from a demagnetized magnet ($H = M = 0$). To simulate this curve in a valley-polarized system, we use such an expression:

$$h_v = \frac{U_v}{4\mathcal{V}} \sum_{k,\tau,\tau'} \tau f(\epsilon_{k,\tau} - \tilde{\mu}^0 - \frac{eV}{2}\mathrm{sgn}(\epsilon'_{k,\tau}) - h_v^0 \tau\tau'). \tag{B.9}$$

Here $\tau' = \pm$. Actually, this expression is an average of the initial positive valley polarization h_v^0 state and initial negative valley polarization $-h_v^0$ state, which can be used to simulate a demagnetized state, roughly. When the current is absent ($eV = 0$), h_v will be zero. In detail, the parameter a is evaluated as:

$$\begin{aligned}
a &= \left.\frac{\partial h_v}{\partial I_{ext}}\right|_{I_{ext}=0} = \left.\frac{\partial h_v}{\partial eV}\right|_{eV=0} \left.\frac{\partial eV}{\partial I_{ext}}\right|_{I_{ext}=0} \\
&= -\frac{U_v}{4\mathcal{V}} \sum_{k,\tau} \tau f(\epsilon_{k,\tau} - \tilde{\mu}^0 - h_v^0\tau) \frac{\mathrm{sgn}(\epsilon'_{k,\tau})}{2}\gamma \\
&- \frac{U_v}{4\mathcal{V}} \sum_{k,\tau} \tau f(\epsilon_{k,\tau} - \tilde{\mu}^0 + h_v^0\tau) \frac{\mathrm{sgn}(\epsilon'_{k,\tau})}{2}\gamma \\
&= -\frac{U_v}{4\mathcal{V}} \sum_{k,\tau} \tau f(\epsilon_{k,\tau} - \tilde{\mu}^0 - h_v^0\tau) \frac{\mathrm{sgn}(\epsilon'_{k,\tau})}{2}\gamma \\
&- \frac{U_v}{4\mathcal{V}} \sum_{-k,-\tau} (-\tau) f(\epsilon_{-k,-\tau} - \tilde{\mu}^0 + (-\tau)h_v^0) \frac{\mathrm{sgn}(\epsilon'_{-k,-\tau})}{2}\gamma \\
&= -\frac{U_v}{4\mathcal{V}} \sum_{k,\tau} \tau f(\epsilon_{k,\tau} - \tilde{\mu}^0 - h_v^0\tau)\mathrm{sgn}(\epsilon'_{k,\tau})\gamma.
\end{aligned} \tag{B.10}$$

Here we use the relation: $\epsilon_{k,\tau} = \epsilon_{-k,-\tau}$ and $\epsilon'_{k,\tau} = -\epsilon'_{-k,-\tau}$. Referring to our derivation of Eq. (A.4), the parameter γ is:

$$\begin{aligned}
\gamma &= \left.\frac{\partial eV}{\partial j_{ext}}\right|_{j_{ext}=0} \\
&\approx \frac{h}{e} \sum_{\tau} [-f(\epsilon_{k,\tau}^{max} - \tilde{\mu}^0 - h_v^0\tau) + f(\epsilon_{k,\tau}^{min} - \tilde{\mu}^0 - h_v^0\tau)]^{-1}.
\end{aligned} \tag{B.11}$$

Substituting Eq. (B.11) into Eq. (B.10), we can find the value of a is just equal to the value of $\frac{U_v}{2\mathcal{V}}(\alpha_+ - \alpha_-)$ as shown in Eq. (A.7), in view of $\tilde{\mu} = \tilde{\mu}^0$ and $h_v = h_v^0$ at $j_{ext} = 0$ ($eV = 0$). For the parameter b, it is related to the irreversible part of the initial magnetization curve and cannot be evaluated easily. However, we can assume a case for soft materials where the coercive field j_{ext}^c is very small [75]. The coercive field j_{ext}^c is the zero point of the function

$h_v(j_{ext})$, satisfying $(a+bj_{ext,m})j_{ext}^c \pm \frac{b}{2}(j_{ext,m}^2-(j_{ext}^c)^2)=0$. We take the case for '+' as an example (the case for '−' is similar) and get:

$$j_{ext}^c = \frac{(a+bj_{ext,m})-a\sqrt{1+2\frac{b}{a}j_{ext,m}+2\frac{b^2}{a^2}j_{ext,m}^2}}{b}. \tag{B.12}$$

By using the condition of soft materials ($|j_{ext}^c|$ is small), we deduce that $\frac{b}{a}j_{ext,m} \ll 1$ from Eq. (B.12). Therefore, in the case of soft materials, $a \gg bj_{ext,m}$, Eq. (B.8b) can be simplified as: $h_v(j_{ext}) = aj_{ext} \pm \frac{b}{2}j_{ext,m}^2 = aj_{ext} \pm h_v^0$. This just corresponds to the linear relation shown in Eq. (5) in the main text.

Additionally, even if we expand the function in Eq. (B.9) into the second order of I_{ext}, we can find the expansion coefficient:

$$\begin{aligned}\tilde{b} \equiv \left.\frac{\partial^2 h_v}{\partial^2 j_{ext}}\right|_{j_{ext}=0} &= \left.\frac{\partial^2 h_v}{\partial^2 eV}\gamma^2\right|_{eV=0} \\ &= \frac{U_v\gamma^2}{16\mathcal{V}}\sum_{k,\tau}\tau f''(\epsilon_{k,\tau}-\tilde{\mu}^0-h_v^0\tau) \\ &+ \frac{U_v\gamma^2}{16\mathcal{V}}\sum_{k,\tau}\tau f''(\epsilon_{k,\tau}-\tilde{\mu}^0+h_v^0\tau) \\ &= 0.\end{aligned} \tag{B.13}$$

Although not rigorously, Eq. (B.13) implies that the coefficient b is small at the bias $eV=0$. This is some justification to assume $bI_{ext,m} \ll a$ in our case.

In summary, from two fashioned theoretical perspectives, we demonstrate that the linear approximation between h_v and j_{ext} in Eq. (5) is still plausible when j_{ext} is relatively small, even though the effect of current or voltage is taken into account in the self-consistent process. Once j_{ext} becomes too large, the weak equilibrium of valley-dependent electron occupations can indeed be broken, and the total valley polarization will be reversed by the flowing current. But in principle, as long as the intersection points shown in Fig. 3 exist before valley flip happens, our physical picutures are still qualitatively valid.

C The effect of trigonal warping effect

Trigonal warping is a fundamental effect of the energy bands for graphene and (twisted) multilayer graphene systems, which means that the originally rotationally symmetrical Fermi contour (isoenergetical line) is deformed into a shape like the triangle/triangle star, reflecting C_{3z} symmetry of the system [62, 80, 81]. In some special cases, the trigonally warped closed Fermi surface may be further broken into three disconnected pockets, which corresponds to a so-called Lifshitz transformation [58, 82].

In realistic graphene and (twisted) multilayer graphene systems, the trigonal warping effect is one origin of the broken intravalley inversion symmetry within each two-dimensional (2D) valley band. Regardless of whether the Fermi surface has been broken into three pockets, the trigonally warped bands can allow the current-induced valley polarization modulation and the finite-momentum Cooper pairs with a three-fold degeneracy. To see this, we here take a low-energy effective 2D continuum bands $E_{k_x,k_y,\tau}$ near the $\mathbf{\Gamma_m}$ point of the moiré Brillouin zone. A related and more comprehensive tight-binding model will be further presented in Appendix. E. The discussion is basically similar for other twisted multilayer graphene systems. The 2D valley bands $E_{k_x,k_y,\tau}$ with a finite valley splitting h_v can be written as [61, 83]:

$$E_{k_x,k_y,\tau}^{eff} = \epsilon_{k_x,k_y,\tau}^{eff} - \tau h_v - \tilde{\mu} = \lambda_0(k_x^2+k_y^2) + \tau\lambda_1 k_x(k_x^2-3k_y^2) - \tau h_v - \tilde{\mu} \tag{C.1}$$

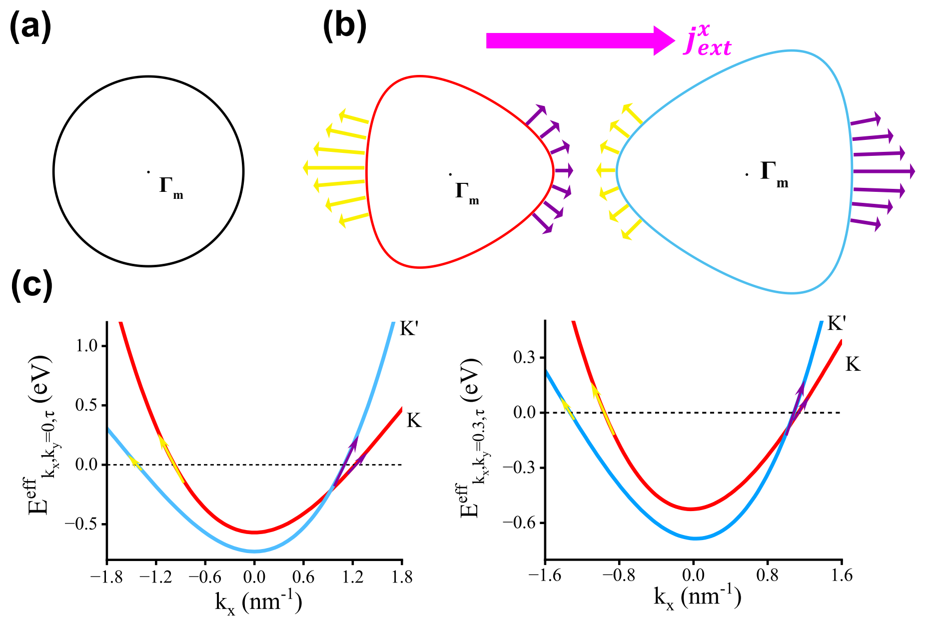

Figure 7: (a) The schematic diagram for an isotropically circular Fermi contour of E^{eff}_{τ} around Γ_m point with $\lambda_1 = 0$. (b) The schematic diagram for typically trigonally warped Fermi contours around Γ_m point of E^{eff}_{τ} with $\lambda_1 \neq 0$. The red/blue color denotes K/K' valley, which are plotted separately for clarity. Purple arrows and yellow arrows schematically indicate local Fermi velocities of right and left movers, respectively. The electric current j^x_{ext} is applied along x direction. (c) the effective 1D valley bands $E^{eff}_{k_x,k_y,\tau}$ for the fixed $k_y = 0$ (left panel) and $k_y = 0.3$ nm^{-1} (right panel). The colored arrows also schematically indicate amplitudes of local Fermi velocities of effective 1D bands at the Fermi level (dark dashed lines). Here the model parameters (with units) are chosen as $\lambda_0 = 0.5$ eV nm^2, $\lambda_1 = -0.1$ eV nm^3, $\tilde{\mu} = 0.65$ eV, $h_v = -0.08$ eV.

The parameters λ_0 and λ_1 denote the kinetic coefficient and trigonal warping coefficient, respectively. $\mathbf{k} = (k_x, k_y)$ is the wave vector relative to the $\mathbf{\Gamma_m}$ point in the moiré Brillouin zone. Actually, the effective low-energy band E^{eff}_{τ} can be also rewritten in polar coordinates: $E^{eff}_{k_r,\phi,\tau} = \lambda_0 k_r^2 + \lambda_1 k_r^3 \cos(3\phi)\tau_z - \tau h_v - \tilde{\mu}$ with the radial wave vector $k_r = \sqrt{k_x^2 + k_y^2}$ and the polar angle ϕ. We can see the term $\cos(3\phi)$ indeed indicates a three-fold symmetry.

In Figs. 7(a,b), we schematically demonstrate two typical types of Fermi contours of $E^{eff}_{k_x,k_y,\tau}$ close to Γ_m point with and without the trigonal warping effect. Compared to the isotropically circular Fermi contour ($\lambda_1 = 0$) [Fig. 7(a)], the trigonally warped Fermi contour has been deformed into a triangle-like shape with C_{3z} symmetry ($\lambda_1 \neq 0$) [Fig. 7(b)]. Additionally, we use red and blue colors to distinguish K band and K' band (plotted separately) in Fig. 7(b), and use distinct sizes of Fermi contours to imply a finite valley splitting. When applying an electric current j^x_{ext} in the bulk along the x direction, the Fermi level of right movers and left movers should be respectively lifted and declined by the electric voltage. Due to the asymmetry of trigonally warped Fermi contours, we can find the cases of Fermi velocities for right movers (purple arrows) and left movers (yellow arrows) are evidently different, which may also lead to a variation of the carrier occupation within each valley. For convenience, we simply fix the quantum number k_y and regard the 2D effective model as an 1D effective model [61]. Due to the symmetry breaking $E^{eff}_{k_x,\tau} \neq E^{eff}_{-k_x,\tau}$, the Fermi velocities along x direction for right movers $v^+_{F,\tau}$ and right movers $v^-_{F,\tau}$ is usually unequal, which is quite similar to Fig. 1(a) in our manuscript. In Fig. 7(c), we respectively show the 1D effective bands $E^{eff}_{\tau}(k_x)$ for $k_y = 0$ (left panel) and $k_y = 0.3$ nm^{-1} (right panel). They all exhibit asymmetrical feature with unequal Fermi velocities (colored arrows) at the Fermi level (dark dashed lines). Due to the time reversal relation between K band and K' band ($E^{eff}_{k_x,\tau} = E^{eff}_{-k_x,-\tau}$), the relative relationship between Fermi velocities of left movers and right movers is also opposite. For example, in Fig. 7(c), $v^+_{F,\tau} < v^-_{F,\tau}$ for $\tau = +$ (red band) while $v^+_{F,\tau} > v^-_{F,\tau}$ for $\tau = -$ (blue band). This guarantees the opposite modulation of electron occupations induced by the electric currents in two valley bands.

We can also generalize the formulas for current-induced valley polarization modulations in Appendix. A from 1D model to 2D model. Considering an applied current j^x_{ext} along x direction with a bias V, the electron occupation n and normal current j^x_{ext} can be respectively written as:

$$\begin{cases} n_\tau = \sum_{k_y,k_x} f[E^{eff}_{k_x,k_y,\tau} - \frac{eV}{2}\mathrm{sgn}(\frac{\partial E^{eff}_\tau}{\partial k_x})] \\ j^x_{ext} = \frac{e}{\hbar\mathcal{V}} \sum_{k_y,k_x,\tau} \frac{\partial E^{eff}_\tau}{\partial k_x} f[E^{eff}_{k_x,k_y,\tau} - \frac{eV}{2}\mathrm{sgn}(\frac{\partial E^{eff}_\tau}{\partial k_x})] \end{cases} \tag{C.2}$$

Compared to formulas for 1D model, the formulas for 2D model additionally involves the summation over the quantum number k_y. Here $\mathcal{V}$ represents the size of the 2D system. Similarly, considering a small bias $V \to 0$, we can still derive a linear relation between n_τ, h_v and j^x_{ext} (sheet current density), by using a Taylor expansion of eV:

$$\begin{cases} n_\tau \approx n^0_\tau + \alpha^x_\tau j^x_{ext} \\ h_v = \frac{U_v}{2\mathcal{V}}(n_+ - n_-) \approx \frac{U_v}{2\mathcal{V}}(\alpha^x_+ - \alpha^x_-) j^x_{ext} + h^0_v \end{cases} \tag{C.3}$$

The n^0_τ and h^0_v denote the initial electron number and valley spitting without the applied current, respectively. The coefficient α^x_τ can be arranged as:

$$\alpha^x_\tau = \frac{\mathcal{V}\hbar}{e} \frac{\sum_{k_x,k_y} f'(E^{eff}_{k_x,k_y,\tau})\mathrm{sgn}(\frac{\partial E^{eff}_\tau}{\partial k_x})}{\sum_{k_x,k_y,\tau} \frac{\partial E^{eff}_\tau}{\partial k_x} f'(E^{eff}_{k_x,k_y,\tau})\mathrm{sgn}(\frac{\partial E^{eff}_\tau}{\partial k_x})} \tag{C.4}$$

For the zero temperature limit and small bias, we can simply approximate the modulation of electron occupation Δn_τ for valley τ as:

$$\Delta n_\tau = n_\tau - n^0_\tau \approx \frac{\mathcal{V}}{(2\pi)^2} \frac{eV}{2} \times (\int_{l_1} \frac{dl}{|\nabla_{\mathbf{k}} E_\tau|} - \int_{l_2} \frac{dl}{|\nabla_{\mathbf{k}} E_\tau|}) \tag{C.5}$$

Here l_1 and l_2 represent the part of Fermi contour for right movers (purple arrows) and left movers (yellow arrows), respectively. $|\nabla_{\mathbf{k}} E_\tau|$ is related to the magnitude of local Fermi velocity. Since the trigonal warping breaks intravalley inversion symmetry, the subtraction between two integrals in Eq. (C.5) is generally nonzero. A finite bias (electric current) can thus induce the modulation of electron occupation in one valley.

D The coupling between supercurrents and valley polarizations

In Fig. 1(a) of the main text, we have demonstrated the normal-current-induced valley polarization modulation. The key point is nonequilibrium Fermi levels for moving forward and backward electrons. In this section, we will demonstrate that even an equilibrium supercurrent can also couple to valley polarizations.

In detail, when the system enters the superconducting phase, the supercurrent j_s is no longer driven by the finite electric voltage V but instead carried by finite-momentum Cooper

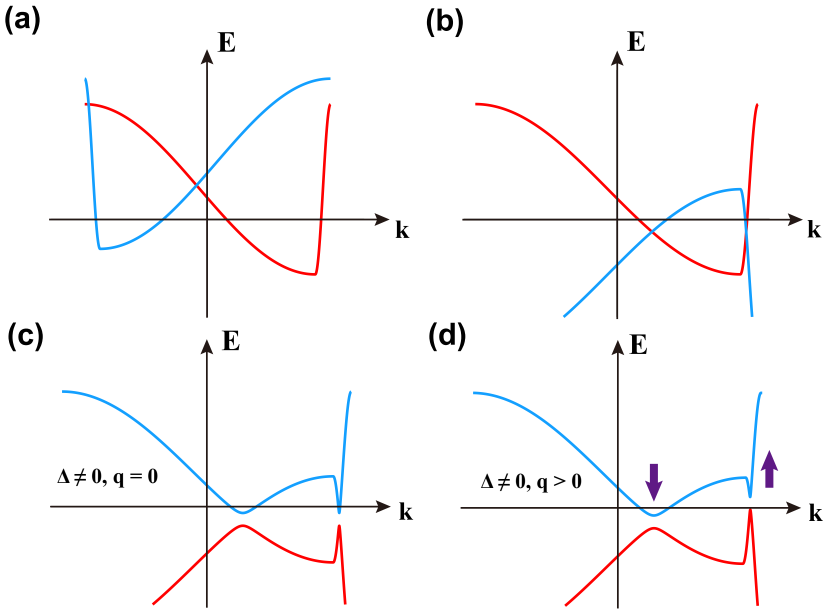

Figure 8: (a) The schematic diagram for 1D effective valley bands $E_{k,+}$ (red color) and $E_{k,-}$ (blue color) with a finite valley splitting $h_v > 0$. (b) The schematic diagram for K band $E_{k,+}$ (red color) and K' band $-E_{-k,-}$ (blue color) based on the BdG transformation. (c) The schematic diagram for Bogoliubov quasiparticle bands $\tilde{E}_+(k)$ (blue color) and $\tilde{E}_-(k)$ (red color) with a fixed superconducting order parameter $\Delta \neq 0$. (c) The schematic diagram for Bogoliubov quasiparticle bands $\tilde{E}_+(k,q)$ (blue color) and $\tilde{E}_-(k,q)$ (red color) with a fixed superconducting order parameter $\Delta \neq 0$ and a finite momentum $q > 0$. The purple arrows indicate band shifts, depending on band dispersions of $E_{k,+}$.

pairs. In other words, the coupling between the valley polarization and supercurrents is equal to discuss the influences of the Cooper-pair momentum $2q$ and the superconducting order parameter Δ on h_v. To investigate this effect, we simultaneously consider the inter-valley repulsive interaction and inter-valley superconducting pairing in the Hamiltonian, and treat them simultaneously in the mean-field approximation [44]. Thereby, the total free energy F_t should be a combination of free energies shown in Eq. (2) and Eq. (8). It will be a function of order parameters $\Delta(q)$, h_v and also the momentum q:

$$F_t(q,\Delta(q),h_v) = -T \sum_{k,\eta=\pm} \ln(1+e^{-\frac{\tilde{E}_\eta(k,q)}{T}}) + \sum_k E_{-k+q,-} + \frac{\mathcal{V}\Delta(q)^2}{U_s} + \frac{\mathcal{V}h_v^2}{U_v} - \frac{U_v}{\mathcal{V}}n^2 + \mu n \quad \text{(D.1)}$$

Note that the parameters in Eq. (D.1) are parallel to those in Eq. (2) and Eq. (8). For simplicity, we set the averaged total electron number n and the chemical potential μ as constants, which will not influence the total free energy F_t.

To keep the system in the minimum point of the free energy, we demand that the first-order derivatives of F_t with respect to h_v and Δ are both zero for the fixed q. These lead to a set of self-consistent equations:

$$\begin{cases} \frac{\partial F_t(q,\Delta,h_v)}{\partial h_v} = 0, \\ \frac{\partial F_t(q,\Delta,h_v)}{\partial \Delta} = 0, \end{cases} \Rightarrow \begin{cases} h_v(\Delta,q) = \frac{U_v}{2\mathcal{V}} \sum_k \left[f(\tilde{E}_-(k,q)) - f(-\tilde{E}_+(k,q)) \right], \\ \Delta(q,h_v) = -\frac{U_s}{\mathcal{V}} \sum_k \frac{\Delta(q,h_v)}{2\sqrt{E_2^2(k,q)+\Delta^2(q,h_v)}} [f(\tilde{E}_+(k,q)) - f(\tilde{E}_-(k,q))]. \end{cases} \quad \text{(D.2)}$$

Compared to Eq. (3) in the main text, it can be found that the first line of Eq. (D.2) has corrected the self-consistent expression for h_v, where the occupation difference between two valley bands $E_{k,\pm}$ is replaced by the occupation difference between two Bogoliubov quasiparticle bands $\tilde{E}_-(k,q)$ and $-\tilde{E}_+(k,q)$. Once the superconducting order parameter Δ becomes zero (in the normal phase), the self-consistent equation for h_v in Eq. (D.2) can be verified to be the same as Eq. (3) and the physical picture just returns to Fig. 1(a). Especially, once Δ becomes very large, the Bogoliubov quasiparticle band $\tilde{E}_-(k,q) = E_1(k,q) - \sqrt{E_2^2(k,q)+\Delta^2(q)}$ will be totally negative while $\tilde{E}_+(k,q) = E_1(k,q) + \sqrt{E_2^2(k,q)+\Delta^2(q)}$ will be totally positive. This indicates the summation of $\sum_k f(\tilde{E}_-(k,q))$ and $-\sum_k f(-\tilde{E}_+(k,q))$ will be exactly canceled, resulting a zero h_v. This phenomenon reflects that the formation of superconducting Cooper pairs will suppress the valley polarization.

Restricting to the single-q order parameter, the supercurrent $J_s(q)$ is approximately proportional to $|\Delta|^2 q$ near the superconducting phase transition [42]. In view of this, to investigate the effect of supercurrents j_s on valley polarizations, we consider a non-zero order parameter Δ and focus on the effect of q on h_v. Assuming q is a small quantity, we perform a Taylor expansion for the right part of the first-line equation in Eq. (D.2):

$$h_v(\Delta,q) \approx h_v(\Delta,q=0) + \beta(\Delta,q=0)q + O(q^2). \tag{D.3}$$

Here the first-order expansion coefficient $\beta(\Delta,q=0)$ is derived as:

$$\begin{aligned}\beta(\Delta,q=0) &= \frac{U_v}{2\mathcal{V}}\sum_k\left[f'(\tilde{E}_-(k,q=0))\frac{\partial\tilde{E}_-(k,q)}{\partial q}\bigg|_{q=0} + f'(\tilde{E}_+(k,q=0))\frac{\partial\tilde{E}_+(k,q)}{\partial q}\bigg|_{q=0}\right]\\ &= \frac{U_v}{2\mathcal{V}}\sum_k[f'(\tilde{E}_+(k,q=0)) + f'(\tilde{E}_-(k,q=0))]\epsilon'_{k,+}\end{aligned} \tag{D.4}$$

In Eq. (D.4), we can find the the first-order expansion coefficient $\beta(\Delta,q=0)$ is still related to the energy band dispersion $\epsilon'_{k,+}$, which is somehow consistent with the linear expansion coefficient α_τ in Eq. (A.7). Especially, when the valley bands preserve intravalley inversion symmetry: $\epsilon_{k,\tau} = \epsilon_{-k,\tau}$, the summation in Eq. (D.4) will automatically be canceled, indicating that the finite Cooper-pair momentum $2q$ is uneasy to influence h_v. In short, Eq. (D.4) demonstrates a relation where the valley polarization is approximately proportional to the finite Cooper-pair momentum $2q$ and also the corresponding supercurrent $j_s \propto q$.

The similarity between the finite-momentum-induced valley polarization modulation in Eq. (D.2) and the voltage-induced valley polarization modulation in Eq. (A.6) can be also elucidated from the BdG Hamiltonian. Performing the Taylor expansion of q, the origin BdG Hamiltonian $H(q)$ can be rewritten as:

$$\begin{aligned}H(q) &= \sum_k (c^\dagger_{k+q,+}, c_{-k+q,-})\begin{pmatrix} E_{k+q,+} & -\Delta(q) \\ -\Delta(q) & -E_{-k+q,-}\end{pmatrix}\begin{pmatrix} c_{k+q,+} \\ c^\dagger_{-k+q,-}\end{pmatrix}\\ &= \sum_k (c^\dagger_{k+q,+}, c_{-k+q,-}),\begin{pmatrix} \epsilon_{k+q,+} - \tilde{\mu} - h_v & -\Delta(q) \\ -\Delta(q) & -\epsilon_{k-q,+} + \tilde{\mu} - h_v\end{pmatrix}\begin{pmatrix} c_{k+q,+} \\ c^\dagger_{-k+q,-}\end{pmatrix}\\ &\approx \sum_{k,\tau} (c^\dagger_{k+q,+}, c_{-k+q,-}),\begin{pmatrix} \epsilon_{k,+} + \epsilon'_{k,+}q - \tilde{\mu} - h_v & -\Delta(q) \\ -\Delta(q) & -\epsilon_{k,+} + \epsilon'_{k,+}q + \tilde{\mu} - h_v\end{pmatrix}\begin{pmatrix} c_{k+q,+} \\ c^\dagger_{-k+q,-}\end{pmatrix}.\end{aligned} \tag{D.5}$$

In Eq. (D.5), although the finite Cooper-pair momentum does not induce a non-equilibrium electron distribution similar to Fig. 1(a), it effectively alters the band structure by an energy

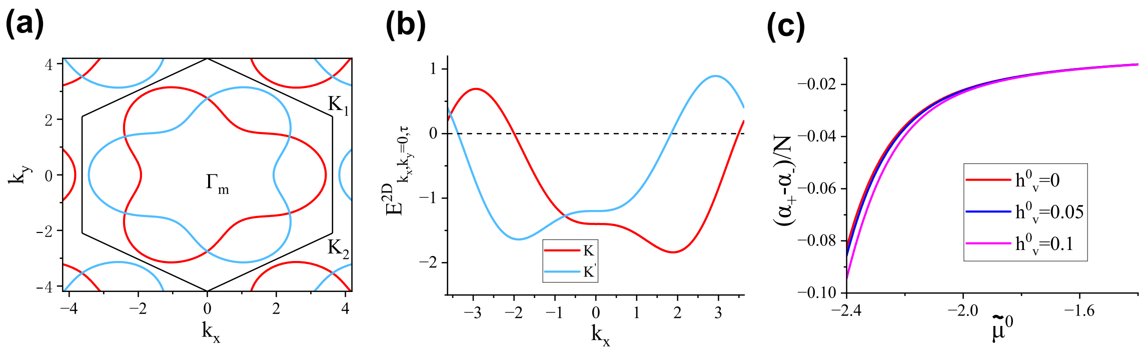

Figure 9: (a) The trigonally-warped Fermi surfaces of $H^{2D}_{\tau}(k_x, k_y)$ for effective twisted bilayer graphene bands with $t_1 = 1, t_2 = 0.05, t'_2 = 0.2, h_v = 0$ and $\mu = -1.4$. The red and blue Fermi surfaces denote K and K' valley, respectively. The hexagonal frame mark the moiré Brillouin zone. Note that k_x and k_y are in the units of L_M^{-1}. Here L_M is the moiré lattice constant and be set to $L_M = 1$ in calculations. (b) The 1D effective valley bands of $E^{2D}_{k_x,k_y=0,\tau}$ of H^{2D}_{τ} with a finite valley splitting field $h_v = 0.1$. (c) The change of modulation coefficient $(\alpha_+ - \alpha_-)/N$ versus the initial chemical potential $\tilde{\mu}^0$ for several initial valley splitting field h^0_v. Here the coefficient α_τ is in the unit of $h/2et_1$.

shift $\epsilon'_{k,+}q$, which still depends on the sign of band dispersions. Taking 1D effective valley bands shown in Fig. 1(a) as an example, in Fig. 8, we schematically demonstrate the effect of this energy shift. In Fig. 8(a), the K valley band $E_{k,+} = \epsilon_{k,+} - \tilde{\mu} - h_v$ (red color) and K' valley band $E_{k,-} = \epsilon_{k,-} - \tilde{\mu} + h_v$ (blue color) are respectively plotted with a finite valley splitting $h_v > 0$. In Fig. 8(b), we convert the K' valley band $E_{k,-}$ into $-E_{-k,-}$ corresponding to the BdG transformation in Eq. (D.5). By introducing a finite superconducting order parameter $\Delta \neq 0$, the superconducting gap will open, and the K and K' valley bands are recombined into two Bogoliubov quasiparticle bands $\tilde{E}_+(k)$ (blue color) and $\tilde{E}_-(k)$ (red color). According to Eq. (D.2), the valley polarization is now related to the occupation difference between $\sum_k f(\tilde{E}_-(k))$ and $\sum_k f(-\tilde{E}_+(k))$. Especially, considering a contribution of the small momentum q, the energy shift $\epsilon'_{k,+}q$ will break the alignment of right and left parts of BdG bands. See Fig. 8(d), a finite momentum q respectively induces downward and upward energy shift (purple arrows) around right and left crossing points between $E_{k,+}$ and $E_{-k,-}$. When valley bands possess intravalley inversion symmetry, the downward and upward energy shifts should be equal and the occupations on each Bogoliubov quasiparticle band $\tilde{E}_-(k,q)$ and $-\tilde{E}_+(k,q)$ are approximately unchanged, also making valley polarizations still. Conversely, when intravalley inversion symmetry has been broken, the unequal band dispersions indicate opposing energy shifts cannot be equal, and the occupations on each Bogoliubov quasiparticle band $\tilde{E}_-(k,q)$ and $-\tilde{E}_+(k,q)$ can be changed. Moreover, the variations of occupations on two Bogoliubov quasiparticle bands may also not be offset [e.g., Fig. 8(d)], thereby modulating h_v based on Eq. (D.2).

E The estimation of $\alpha_\pm$ in a more realistic tight-binding model and the effect of band asymmetry

In numerical calculations of the main text, we pick an 1D effective toy model to generally demonstrate the broken intravalley inverison symmetry will lead to current-induced valley polarization modulations. Actually, in some more realistic system, the parameters for $\alpha_\pm$ in

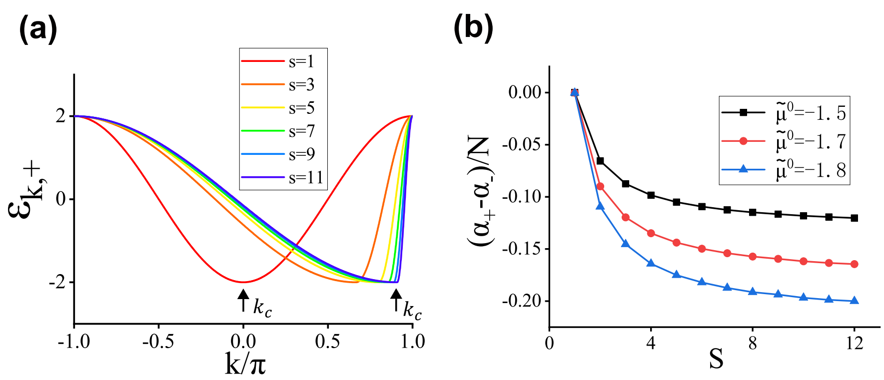

Figure 10: (a) A series of K bands with distinct band asymmetries characterized by s. The K' bands are just their TRS counterparts and not shown here. k_c denotes the position of the local minimum for the energy band. (b) the change of coefficient $(\alpha_+ - \alpha_-)/N$ as a function of s for different $\tilde{\mu}^0$ with $h_v^0 = 0.1$.

Eq. (A.6) are likewise significant. Here we use a tight-binding Hamiltonian on the honeycomb lattice with (p_x, p_y) orbitals which are often used to simulate the four lowest moiré bands of twisted bilayer graphene [61, 84, 85]. It is written as:

$$H_\tau^{2D} = \sum_{\langle ij \rangle} t_1 c_{i,\tau}^\dagger c_{j,\tau} + \sum_{\langle ij \rangle'} (t_2 - i\tau t_2') c_{i,\tau}^\dagger c_{j,\tau} + \text{H.c.} - \sum_{i,\tau} (\tilde{\mu} + \tau h_v) c_{i,\tau}^\dagger c_{i,\tau}. \tag{E.1}$$

where $\langle ij \rangle$ denotes the nearest-neighbor hopping terms with the hopping energy t_1, $\langle ij \rangle'$ denotes the fifth nearest-neighbor hopping terms with the hopping energy t_2 and t_2'. $c_{i,\tau}^\dagger$ and $c_{i,\tau}$ respectively denote the creation and annihilation operator for the electron at the lattice site i with $p_x + i\tau p_y$ orbital ($\tau = \pm$ represent K and K' valley). Actually, the low-energy effective 2D continuum valley bands in Appendix. C are just derived from an expansion of H_τ^{2D} at Γ_m point where λ_0 is directly related to t_1 and t_2, λ_1 is directly related to t_2' [61, 83, 84]. Similar to the procedure in our main text, we choose t_1 as the energy unit ($t_1 = 1$), and set $t_2 = 0.05t_1$ and $t_2' = 0.2t_1$ according to the previous Reference [61]. Usually, for magic-angle twisted bilayer graphene, the hopping energy of t_1 roughly corresponds to 4 meV [61]. Note that t_2' characterizes the trigonal warping effect, as is shown by the triangular-shaped Fermi surfaces of $H_\tau^{2D}(k_x, k_y)$ in Fig. 9(a). It is evident for twisted bilayer graphene bands to break the intravalley inversion symmetry.

For simplicity, we also fix $k_y = 0$ and reduce the 2D energy bands of Ttwisted bilayer graphene as an 1D energy band. In Fig. 9(b), we plot two valley bands $E_{k_x,k_y=0,\tau}^{2D}$ near the Fermi surface with a initial finite valley splitting h_v. Similar to Fig. 1(a), we can see they both exhibit an evident band asymmetry: $E_{k_x,k_y=0,\tau}^{2D} \neq E_{-k_x,k_y=0,\tau}^{2D}$. Analogous to Fig. 1(c), we use Eq. (A.7) to calculate the modulation coefficient $(\alpha_+ - \alpha_-)/N$ of the 1D energy band $E_{k_x,k_y=0,\tau}^{2D}$ versus the initial chemical potential $\tilde{\mu}^0$ for several initial valley splitting field h_v^0. Here $T = 0.1t_1$ and $N = 2000$ corresponds to the number of discrete k_x points. It can be found that $(\alpha_+ - \alpha_-)/N$ has demonstrated relatively large values at some chemical potentials.

In addition, in Fig. 10, we also investigate how the band asymmetry affects $\alpha_+ - \alpha_-$. In Fig. 10(a), a series of 1D K valley bands are considered: $\epsilon_{k,+} = -2t\cos[\frac{s}{2s-1}(k - \frac{s-1}{s}\pi)]$ for $-\pi \leq k \leq \frac{(s-1)}{s}\pi$ and $\epsilon_{k,+} = -2t\cos(sk - \pi) \times (-1)^s$ for $\frac{(s-1)}{s}\pi < k < \pi$. Note that $\epsilon_{k,-} = \epsilon_{-k,+}$. Here s is introduced to denote the location of the wavevector for the global minimum $k_c = \frac{s-1}{s}\pi$ [see Fig. 10(a)]. As s increases from 1, k_c tends to be close to π and the energy band $\epsilon_{k,\tau}$ becomes more asymmetric. For the calculations in the main text, s is set

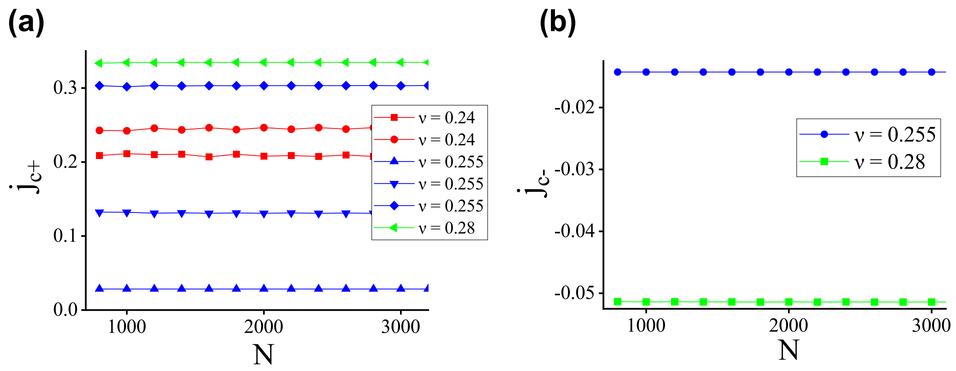

Figure 11: (a,b) the change of actual critical currents j_{c+} (a) and j_{c-} (b) as a function of the system size N for the fixed proportion of the number of electrons $\upsilon = 0.24, 0.255, 0.28$.

as $s = 8$. In Fig. 10(b), under an fixed initial valley splitting field $h_v^0 = 0.1$, the magnitude of $(\alpha_+ - \alpha_-)/N$ shows an apparent tendency to grow as s climbs, see Fig. 10(b) for three different $\tilde{\mu}$. Since a larger coefficient $\alpha_+ - \alpha_-$ implies the current j_{ext} can weaken the valley polarization h_v faster, more asymmetric energy bands are more likely to induce the extreme nonreciprocity.

F The convergence of results for the system size

In principle, as long as the proportion of the number of electrons (the filling factor) $\upsilon = n/N$ in the system is fixed, our conclusions in the main text should remain unchanged as $N \to \infty$. To confirm our calculations have converged, we increase the system size Na $(a = 1)$ by fixing $\upsilon = 0.24, 0.255, 0.28$ respectively. The changes of actual critical current j_{c+} and j_{c-} as a function of N are shown in Fig. 11, respectively. Actually, $\upsilon = 0.24$ corresponds to $n = 480$ when $N = 2000$ [Fig. 3(d)] where the system enters an extreme nonreciprocity only with two positive j_{c+} [red lines in Fig. 11(a)]. $\upsilon = 0.255$ corresponds to $n = 510$ with $N = 2000$ [Fig. 3(c)] and the system enters the re-entrant superconductivity with four distinct critical currents j_c [dark blue lines in Figs. 11(a,b)]. $\upsilon = 0.28$ corresponds to $n = 560$ with $N = 2000$ [Fig. 3(b)] where the system enters the conventional SDE with $j_{c+} > 0$ and $j_{c-} < 0$ [light green lines in Fig. 11]. Fig. 11 clearly indicate actual critical currents j_c remain nearly unchanged as the system size N varies from 800 to 3200.

References

[1] M. Nadeem, M. S. Fuhrer and X. Wang, *The superconducting diode effect*, Nat. Rev. Phys. **5**(10), 558 (2023), doi:10.1038/s42254-023-00632-w.

[2] K. Jiang and J. Hu, *Superconducting diode effects*, Nat. Phys. **18**(10), 1145 (2022), doi:10.1038/s41567-022-01701-0.

[3] A. Maiellaro, M. Trama, J. Settino, C. Guarcello, F. Romeo and R. Citro, *Engineered Josephson diode effect in kinked Rashba nanochannels*, SciPost Phys. **17**, 101 (2024), doi:10.21468/SciPostPhys.17.4.101.

[4] W.-T. Lu, T.-F. Fang, Q. Cheng and Q.-F. Sun, *Electrically controlled field-free josephson diode effect in two-dimensional antiferromagnets*, Phys. Rev. B **112**, 184505 (2025), doi:10.1103/y9sq-sntl.

[5] A. I. Braginski, *Superconductor electronics: status and outlook*, J. Supercond. Nov. Magn. **32**(1), 45 (2019), doi:10.1007/s10948-018-4884-4.

[6] J. Linder and J. W. A. Robinson, *Superconducting spintronics*, Nat. Phys. **11**(4), 307 (2015), doi:10.1038/nphys3242.

[7] Y. Mao, Q. Yan, Y.-C. Zhuang and Q.-F. Sun, *Universal spin superconducting diode effect from spin-orbit coupling*, Phys. Rev. Lett. **132**, 216001 (2024), doi:10.1103/PhysRevLett.132.216001.

[8] G. Wendin, *Quantum information processing with superconducting circuits: a review*, Rep. Prog. Phys. **80**(10), 106001 (2017), doi:10.1088/1361-6633/aa7e1a.

[9] X. Liu and M. C. Hersam, *2D materials for quantum information science*, Nat. Rev. Mater. **4**(10), 669 (2019), doi:10.1038/s41578-019-0136-x.

[10] F. Ando, Y. Miyasaka, T. Li, J. Ishizuka, T. Arakawa, Y. Shiota, T. Moriyama, Y. Yanase and T. Ono, *Observation of superconducting diode effect*, Nature (London) **584**(7821), 373 (2020), doi:10.1038/s41586-020-2590-4.

[11] Y. Miyasaka, R. Kawarazaki, H. Narita, F. Ando, Y. Ikeda, R. Hisatomi, A. Daido, Y. Shiota, T. Moriyama, Y. Yanase and T. Ono, *Observation of nonreciprocal superconducting critical field*, Appl. Phys. Express **14**(7), 073003 (2021), doi:10.35848/1882-0786/ac03c0.

[12] Y. M. Itahashi, T. Ideue, Y. Saito, S. Shimizu, T. Ouchi, T. Nojima and Y. Iwasa, *Nonreciprocal transport in gate-induced polar superconductor* $SrTiO_3$, Sci. Adv. **6**(13), eaay9120 (2020), doi:DOI: 10.1126/sciadv.aay9120.

[13] H. Narita, J. Ishizuka, R. Kawarazaki, D. Kan, Y. Shiota, T. Moriyama, Y. Shimakawa, A. V. Ognev, A. S. Samardak, Y. Yanase and T. Ono, *Field-free superconducting diode effect in noncentrosymmetric superconductor/ferromagnet multilayers*, Nat. Nanotechnol. **17**(8), 823 (2022), doi:10.1038/s41565-022-01159-4.

[14] M. Masuko, M. Kawamura, R. Yoshimi, M. Hirayama, Y. Ikeda, R. Watanabe, J. J. He, D. Maryenko, A. Tsukazaki, K. S. Takahashi, M. Kawasaki, N. Nagaosa *et al.*, *Nonreciprocal charge transport in topological superconductor candidate* $Bi_2Te_3/PdTe_2$ *heterostructure*, npj Quantum Mater. **7**(1), 104 (2022), doi:10.1038/s41535-022-00514-x.

[15] J.-X. Lin, P. Siriviboon, H. D. Scammell, S. Liu, D. Rhodes, K. Watanabe, T. Taniguchi, J. Hone, M. S. Scheurer and J. I. A. Li, *Zero-field superconducting diode effect in small-twist-angle trilayer graphene*, Nat. Phys. **18**(10), 1221 (2022), doi:10.1038/s41567-022-01700-1.

[16] L. Bauriedl, C. Bäuml, L. Fuchs, C. Baumgartner, N. Paulik, J. M. Bauer, K.-Q. Lin, J. M. Lupton, T. Taniguchi, K. Watanabe, C. Strunk and N. Paradiso, *Supercurrent diode effect and magnetochiral anisotropy in few-layer* $NbSe_2$, Nat. Commun. **13**(1), 4266 (2022), doi:10.1038/s41467-022-31954-5.

[17] C. Baumgartner, L. Fuchs, A. Costa, S. Reinhardt, S. Gronin, G. C. Gardner, T. Lindemann, M. J. Manfra, P. E. Faria Junior, D. Kochan, J. Fabian, N. Paradiso *et al.*, *Supercurrent rectification and magnetochiral effects in symmetric Josephson junctions*, Nat. Nanotechnol. **17**(1), 39 (2022), doi:10.1038/s41565-021-01009-9.

[18] K.-R. Jeon, J.-K. Kim, J. Yoon, J.-C. Jeon, H. Han, A. Cottet, T. Kontos and S. S. P. Parkin, *Zero-field polarity-reversible Josephson supercurrent diodes enabled by a proximity-magnetized Pt barrier*, Nat. Mater. **21**(9), 1008 (2022), doi:10.1038/s41563-022-01300-7.

[19] H. Wu, Y. Wang, Y. Xu, P. K. Sivakumar, C. Pasco, U. Filippozzi, S. S. P. Parkin, Y.-J. Zeng, T. McQueen and M. N. Ali, *The field-free Josephson diode in a van der waals heterostructure*, Nature (London) **604**(7907), 653 (2022), doi:10.1038/s41586-022-04504-8.

[20] B. Pal, A. Chakraborty, P. K. Sivakumar, M. Davydova, A. K. Gopi, A. K. Pandeya, J. A. Krieger, Y. Zhang, M. Date, S. Ju, N. Yuan, N. B. M. Schröter *et al.*, *Josephson diode effect from cooper pair momentum in a topological semimetal*, Nat. Phys. **18**(10), 1228 (2022), doi:10.1038/s41567-022-01699-5.

[21] F. K. de Vries, E. Portolés, G. Zheng, T. Taniguchi, K. Watanabe, T. Ihn, K. Ensslin and P. Rickhaus, *Gate-defined Josephson junctions in magic-angle twisted bilayer graphene*, Nat. Nanotechnol. **16**(7), 760 (2021), doi:10.1038/s41565-021-00896-2.

[22] J. Díez-Mérida, A. Díez-Carlón, S. Y. Yang, Y. M. Xie, X. J. Gao, J. Senior, K. Watanabe, T. Taniguchi, X. Lu, A. P. Higginbotham, K. T. Law and D. K. Efetov, *Symmetry-broken Josephson junctions and superconducting diodes in magic-angle twisted bilayer graphene*, Nat. Commun. **14**(1), 2396 (2023), doi:10.1038/s41467-023-38005-7.

[23] B. Turini, S. Salimian, M. Carrega, A. Iorio, E. Strambini, F. Giazotto, V. Zannier, L. Sorba and S. Heun, *Josephson diode effect in high-mobility InSb nanoflags*, Nano Lett **22**(21), 8502 (2022), doi:10.1021/acs.nanolett.2c02899.

[24] M. Trahms, L. Melischek, J. F. Steiner, B. Mahendru, I. Tamir, N. Bogdanoff, O. Peters, G. Reecht, C. B. Winkelmann, F. von Oppen and K. J. Franke, *Diode effect in Josephson junctions with a single magnetic atom*, Nature (London) **615**(7953), 628 (2023), doi:10.1038/s41586-023-05743-z.

[25] Y.-Y. Lyu, J. Jiang, Y.-L. Wang, Z.-L. Xiao, S. Dong, Q.-H. Chen, M. V. Milošević, H. Wang, R. Divan, J. E. Pearson, P. Wu, F. M. Peeters *et al.*, *Superconducting diode effect via conformal-mapped nanoholes*, Nat. Commun. **12**(1), 2703 (2021), doi:10.1038/s41467-021-23077-0.

[26] E. Strambini, M. Spies, N. Ligato, S. Ilić, M. Rouco, C. González-Orellana, M. Ilyn, C. Rogero, F. S. Bergeret, J. S. Moodera, P. Virtanen, T. T. Heikkilä *et al.*, *Superconducting spintronic tunnel diode*, Nat. Commun. **13**(1), 2431 (2022), doi:10.1038/s41467-022-29990-2.

[27] J. H. Correa and M. P. Nowak, *Theory of universal diode effect in three-terminal Josephson junctions*, SciPost Phys. **17**, 037 (2024), doi:10.21468/SciPostPhys.17.2.037.

[28] Y. Yerin, S.-L. Drechsler, A. A. Varlamov, M. Cuoco and F. Giazotto, *Supercurrent rectification with time-reversal symmetry broken multiband superconductors*, Phys. Rev. B **110**, 054501 (2024), doi:10.1103/PhysRevB.110.054501.

[29] Q. Cheng and Q.-F. Sun, *Josephson diode based on conventional superconductors and a chiral quantum dot*, Phys. Rev. B **107**, 184511 (2023), doi:10.1103/PhysRevB.107.184511.

[30] G. L. J. A. Rikken, J. Fölling and P. Wyder, *Electrical magnetochiral anisotropy*, Phys. Rev. Lett. **87**, 236602 (2001), doi:10.1103/PhysRevLett.87.236602.

[31] G. L. J. A. Rikken and P. Wyder, *Magnetoelectric anisotropy in diffusive transport*, Phys. Rev. Lett. **94**, 016601 (2005), doi:10.1103/PhysRevLett.94.016601.

[32] R. Wakatsuki and N. Nagaosa, *Nonreciprocal current in noncentrosymmetric Rashba superconductors*, Phys. Rev. Lett. **121**, 026601 (2018), doi:10.1103/PhysRevLett.121.026601.

[33] R. Wakatsuki, Y. Saito, S. Hoshino, Y. M. Itahashi, T. Ideue, M. Ezawa, Y. Iwasa and N. Nagaosa, *Nonreciprocal charge transport in noncentrosymmetric superconductors*, Sci. Adv. **3**(4), e1602390 (2017), doi:10.1126/sciadv.1602390.

[34] J. J. He, Y. Tanaka and N. Nagaosa, *A phenomenological theory of superconductor diodes*, New. J. Phys. **24**(5), 053014 (2022), doi:10.1088/1367-2630/ac6766.

[35] V. Barzykin and L. P. Gor'kov, *Inhomogeneous stripe phase revisited for surface superconductivity*, Phys. Rev. Lett. **89**, 227002 (2002), doi:10.1103/PhysRevLett.89.227002.

[36] K. Michaeli, A. C. Potter and P. A. Lee, *Superconducting and ferromagnetic phases in* $SrTiO_3/LaAlO_3$ *oxide interface structures: Possibility of finite momentum pairing*, Phys. Rev. Lett. **108**, 117003 (2012), doi:10.1103/PhysRevLett.108.117003.

[37] N. F. Q. Yuan and L. Fu, *Topological metals and finite-momentum superconductors*, Proc. Natl Acad. Sci. USA **118**(3), e2019063118 (2021), doi:https://doi.org/10.1073/pnas.2019063118.

[38] H. D. Scammell, J. I. A. Li and M. S. Scheurer, *Theory of zero-field superconducting diode effect in twisted trilayer graphene*, 2D Mater. **9**(2) (2022), doi:10.1088/2053-1583/ac5b16.

[39] Y.-F. Sun, Y. Mao and Q.-F. Sun, *Design of a josephson diode based on double magnetic impurities*, Phys. Rev. B **111**, 054515 (2025), doi:10.1103/PhysRevB.111.054515.

[40] Y.-F. Sun, Y. Mao and Q.-F. Sun, *Design of a josephson diode based on double magnetic impurities*, Phys. Rev. B **111**, 054515 (2025), doi:10.1103/PhysRevB.111.054515.

[41] A. Daido, Y. Ikeda and Y. Yanase, *Intrinsic superconducting diode effect*, Phys. Rev. Lett. **128**, 037001 (2022), doi:10.1103/PhysRevLett.128.037001.

[42] N. F. Q. Yuan and L. Fu, *Supercurrent diode effect and finite-momentum superconductors*, Proc. Natl Acad. Sci. USA **119**(15), e2119548119 (2022), doi:10.1073/pnas.2119548119.

[43] S. Ilić and F. S. Bergeret, *Theory of the supercurrent diode effect in Rashba superconductors with arbitrary disorder*, Phys. Rev. Lett. **128**, 177001 (2022), doi:10.1103/PhysRevLett.128.177001.

[44] S. Banerjee and M. S. Scheurer, *Enhanced superconducting diode effect due to coexisting phases*, Phys. Rev. Lett. **132**, 046003 (2024), doi:10.1103/PhysRevLett.132.046003.

[45] A. Daido and Y. Yanase, *Unidirectional superconductivity and superconducting diode effect induced by dissipation*, Phys. Rev. B **111**, L020508 (2025), doi:10.1103/PhysRevB.111.L020508.

[46] H. Kim, Y. Choi, C. Lewandowski, A. Thomson, Y. Zhang, R. Polski, K. Watanabe, T. Taniguchi, J. Alicea and S. Nadj-Perge, *Evidence for unconventional superconductivity in twisted trilayer graphene*, Nature **606**(7914), 494 (2022), doi:10.1038/s41586-022-04715-z.

[47] Q. Zheng, Y.-C. Zhuang, Q.-F. Sun and L. He, *Coexistence of electron whispering-gallery modes and atomic collapse states in graphene/WSe2 heterostructure quantum dots*, Nat. Commun. **13**(1), 1597 (2022), doi:10.1038/s41467-022-29251-2.

[48] Y. Mao, H.-Y. Ren, X.-F. Zhou, H. Sheng, Y.-H. Xiao, Y.-C. Zhuang, Y.-N. Ren, L. He and Q.-F. Sun, *Orbital hybridization in graphene-based artificial atoms*, Nature **639**(8053), 73 (2025), doi:10.1038/s41586-025-08620-z.

[49] J. D. T. Luna, K. Vilkelis and A. L. R. Manesco, *Probing valley phenomena with gate-defined valley splitters*, SciPost Phys. **18**, 062 (2025), doi:10.21468/SciPostPhys.18.2.062.

[50] Y.-N. Ren, Y.-C. Zhuang, Q.-F. Sun and L. He, *Magnetic-field-tunable valley-contrasting pseudomagnetic confinement in graphene*, Phys. Rev. Lett. **129**, 076802 (2022), doi:10.1103/PhysRevLett.129.076802.

[51] A. L. Sharpe, E. J. Fox, A. W. Barnard, J. Finney, K. Watanabe, T. Taniguchi, M. A. Kastner and D. Goldhaber-Gordon, *Emergent ferromagnetism near three-quarters filling in twisted bilayer graphene*, Science **365**(6453), 605 (2019), doi:10.1126/science.aaw3780.

[52] M. Serlin, C. L. Tschirhart, H. Polshyn, Y. Zhang, J. Zhu, K. Watanabe, T. Taniguchi, L. Balents and A. F. Young, *Intrinsic quantized anomalous Hall effect in a moiré heterostructure*, Science **367**(6480), 900 (2020), doi:10.1126/science.aay5533.

[53] Y. Su and S.-Z. Lin, *Current-induced reversal of anomalous Hall conductance in twisted bilayer graphene*, Phys. Rev. Lett. **125**, 226401 (2020), doi:10.1103/PhysRevLett.125.226401.

[54] X. Ying, M. Ye and L. Balents, *Current switching of valley polarization in twisted bilayer graphene*, Phys. Rev. B **103**, 115436 (2021), doi:10.1103/PhysRevB.103.115436.

[55] W.-Y. He, D. Goldhaber-Gordon and K. T. Law, *Giant orbital magnetoelectric effect and current-induced magnetization switching in twisted bilayer graphene*, Nat. Commun. **11**(1), 1650 (2020), doi:10.1038/s41467-020-15473-9.

[56] C. Huang, N. Wei and A. H. MacDonald, *Current-driven magnetization reversal in orbital Chern insulators*, Phys. Rev. Lett. **126**, 056801 (2021), doi:10.1103/PhysRevLett.126.056801.

[57] U. Zondiner, A. Rozen, D. Rodan-Legrain, Y. Cao, R. Queiroz, T. Taniguchi, K. Watanabe, Y. Oreg, F. von Oppen, A. Stern, E. Berg, P. Jarillo-Herrero *et al.*, *Cascade of phase transitions and Dirac revivals in magic-angle graphene*, Nature (London) **582**(7811), 203 (2020), doi:10.1038/s41586-020-2373-y.

[58] H. Zhou, T. Xie, A. Ghazaryan, T. Holder, J. R. Ehrets, E. M. Spanton, T. Taniguchi, K. Watanabe, E. Berg, M. Serbyn and A. F. Young, *Half- and quarter-metals in rhombohedral trilayer graphene*, Nature (London) **598**(7881), 429 (2021), doi:10.1038/s41586-021-03938-w.

[59] E. C. Stoner and R. Whiddington, *Collective electron specific heat and spin paramagnetism in metals*, Proc. R. Soc. Lond. A **154**(883), 656 (1936), doi:10.1098/rspa.1936.0075.

[60] S. Datta, *Electronic Tansport in Mesoscopic Systems*, Cambridge University Press, England, doi:10.1017/CBO9780511805776 (1995).

[61] J.-X. Hu, Z.-T. Sun, Y.-M. Xie and K. T. Law, *Josephson diode effect induced by valley polarization in twisted bilayer graphene*, Phys. Rev. Lett. **130**, 266003 (2023), doi:10.1103/PhysRevLett.130.266003.

[62] N. J. Zhang, J.-X. Lin, D. V. Chichinadze, Y. Wang, K. Watanabe, T. Taniguchi, L. Fu and J. I. A. Li, *Angle-resolved transport non-reciprocity and spontaneous symmetry breaking in twisted trilayer graphene*, Nat. Mater. **23**(3), 356 (2024), doi:10.1038/s41563-024-01809-z.

[63] P. Fulde and R. A. Ferrell, *Superconductivity in a strong spin-exchange field*, Phys. Rev. **135**, A550 (1964), doi:10.1103/PhysRev.135.A550.

[64] A. I. Larkin and Y. N. Ovchinnikov, *Nonuniform state of superconductors*, Zh. Eksp. Teor. Fiz. **47**, 1136 (1964).

[65] L. Rammelmüller, J. E. Drut and J. Braun, *Pairing patterns in one-dimensional spin- and mass-imbalanced Fermi gases*, SciPost Phys. **9**, 014 (2020), doi:10.21468/SciPostPhys.9.1.014.

[66] In all calculated results, we discard both $I^1_{c\pm}$ as long as one of the $I^1_{c\pm}$ is smaller than 0.01 which roughly corresponds to 1nA for a narrow bandwidth with $4t = 10meV$, considering it is too small to measure in the experiment.

[67] Y. Cao, J. M. Park, K. Watanabe, T. Taniguchi and P. Jarillo-Herrero, *Pauli-limit violation and re-entrant superconductivity in moiré graphene*, Nature (London) **595**(7868), 526 (2021), doi:10.1038/s41586-021-03685-y.

[68] D. Xiao, G.-B. Liu, W. Feng, X. Xu and W. Yao, *Coupled spin and valley physics in monolayers of* MoS_2 *and other Group-VI dichalcogenides*, Phys. Rev. Lett. **108**, 196802 (2012), doi:10.1103/PhysRevLett.108.196802.

[69] B. T. Zhou, K. Taguchi, Y. Kawaguchi, Y. Tanaka and K. T. Law, *Spin-orbit coupling induced valley Hall effects in transition-metal dichalcogenides*, Commun. Phys. **2**(1), 26 (2019), doi:10.1038/s42005-019-0127-7.

[70] Y. Cao, V. Fatemi, A. Demir, S. Fang, S. L. Tomarken, J. Y. Luo, J. D. Sanchez-Yamagishi, K. Watanabe, T. Taniguchi, E. Kaxiras, R. C. Ashoori and P. Jarillo-Herrero, *Correlated insulator behaviour at half-filling in magic-angle graphene superlattices*, Nature (London) **556**(7699), 80 (2018), doi:10.1038/nature26154.

[71] Y. Cao, V. Fatemi, S. Fang, K. Watanabe, T. Taniguchi, E. Kaxiras and P. Jarillo-Herrero, *Unconventional superconductivity in magic-angle graphene superlattices*, Nature (London) **556**(7699), 43 (2018), doi:10.1038/nature26160.

[72] E. Codecido, Q. Wang, R. Koester, S. Che, H. Tian, R. Lv, S. Tran, K. Watanabe, T. Taniguchi, F. Zhang, M. Bockrath and C. N. Lau, *Correlated insulating and superconducting states in twisted bilayer graphene below the magic angle*, Sci. Adv. **5**(9), eaaw9770 (2019), doi:10.1126/sciadv.aaw9770.

[73] V. T. Phong, P. A. Pantaleón, T. Cea and F. Guinea, *Band structure and superconductivity in twisted trilayer graphene*, Phys. Rev. B **104**, L121116 (2021), doi:10.1103/PhysRevB.104.L121116.

[74] H. Zhou, L. Holleis, Y. Saito, L. Cohen, W. Huynh, C. L. Patterson, F. Yang, T. Taniguchi, K. Watanabe and A. F. Young, *Isospin magnetism and spin-polarized superconductivity in Bernal bilayer graphene*, Science **375**(6582), 774 (2022), doi:10.1126/science.abm8386.

[75] S. Blundell, *Magnetism in Condensed Matter*, Oxford University Press, doi:10.1093/oso/9780198505921.001.0001 (2001).

[76] F. Fiorillo, C. Appino and M. Pasquale, *Chapter 1 - Hysteresis in Magnetic Materials*, pp. 1–190, Academic Press, Oxford, doi:10.1016/B978-012480874-4/50019-1 (2006).

[77] G. Bertotti, *Hysteresis in Magnetism*, Academic Press, doi:10.1016/B978-0-12-093270-2.X5048-X (1998).

[78] L. Dante, G. Durin, A. Magni and S. Zapperi, *Low-field hysteresis in disordered ferromagnets*, Phys. Rev. B **65**, 144441 (2002), doi:10.1103/PhysRevB.65.144441.

[79] L. Rayleigh, *Xxv. notes on electricity and magnetism.—iii. on the behaviour of iron and steel under the operation of feeble magnetic forces*, Philos. Mag. **23**(142), 225 (1887), doi:10.1080/14786448708628000.

[80] J. M. Park, Y. Cao, L.-Q. Xia, S. Sun, K. Watanabe, T. Taniguchi and P. Jarillo-Herrero, *Robust superconductivity in magic-angle multilayer graphene family*, Nat. Mater. **21**(8), 877 (2022), doi:10.1038/s41563-022-01287-1.

[81] Y. Cao, D. Rodan-Legrain, J. M. Park, N. F. Q. Yuan, K. Watanabe, T. Taniguchi, R. M. Fernandes, L. Fu and P. Jarillo-Herrero, *Nematicity and competing orders in superconducting magic-angle graphene*, Science **372**(6539), 264 (2021), doi:10.1126/science.abc2836, https://www.science.org/doi/pdf/10.1126/science.abc2836.

[82] A. M. Seiler, F. R. Geisenhof, F. Winterer, K. Watanabe, T. Taniguchi, T. Xu, F. Zhang and R. T. Weitz, *Quantum cascade of correlated phases in trigonally warped bilayer graphene*, Nature **608**(7922), 298 (2022), doi:10.1038/s41586-022-04937-1.

[83] Y.-M. Xie, D. K. Efetov and K. T. Law, *φ_0-josephson junction in twisted bilayer graphene induced by a valley-polarized state*, Phys. Rev. Res. **5**, 023029 (2023), doi:10.1103/PhysRevResearch.5.023029.

[84] N. F. Q. Yuan and L. Fu, *Model for the metal-insulator transition in graphene superlattices and beyond*, Phys. Rev. B **98**, 045103 (2018), doi:10.1103/PhysRevB.98.045103.

[85] M. Koshino, N. F. Q. Yuan, T. Koretsune, M. Ochi, K. Kuroki and L. Fu, *Maximally localized wannier orbitals and the extended hubbard model for twisted bilayer graphene*, Phys. Rev. X **8**, 031087 (2018), doi:10.1103/PhysRevX.8.031087.